



Contents lists available at ScienceDirect

## Remote Sensing of Environment

journal homepage: [www.elsevier.com/locate/rse](http://www.elsevier.com/locate/rse)

# NIR<sub>v</sub>P: A robust structural proxy for sun-induced chlorophyll fluorescence and photosynthesis across scales

Benjamin Dechant<sup>a</sup>, Youngryel Ryu<sup>a,b,\*</sup>, Grayson Badgley<sup>c</sup>, Philipp Köhler<sup>d</sup>, Uwe Rascher<sup>e</sup>, Mirco Migliavacca<sup>f</sup>, Yongguang Zhang<sup>g,h</sup>, Giulia Tagliabue<sup>i</sup>, Kaiyu Guan<sup>i,k</sup>, Micol Rossini<sup>i</sup>, Yves Goulas<sup>l</sup>, Yelu Zeng<sup>m</sup>, Christian Frankenberg<sup>d,n</sup>, Joseph A. Berry<sup>m</sup>

<sup>a</sup> Research Institute of Agriculture and Life Sciences, Seoul National University, Seoul, South Korea

<sup>b</sup> Department of Landscape Architecture and Rural Systems Engineering, College of Agriculture and Life Sciences, Seoul National University, South Korea

<sup>c</sup> Black Rock Forest, Cornwall, NY, USA

<sup>d</sup> Division of Geological and Planetary Sciences, California Institute of Technology, Pasadena, CA, USA

<sup>e</sup> Institute of Bio- and Geosciences, Plant Sciences (IBG-2), Forschungszentrum Jülich GmbH, 52428 Jülich, Germany

<sup>f</sup> Max Planck Institute for Biogeochemistry, Hans Knoll Straße, 10, D-07745 Jena, Germany

<sup>g</sup> International Institute for Earth System Sciences, Nanjing University, Nanjing, Jiangsu 210023, China

<sup>h</sup> Jiangsu Provincial Key Laboratory of Geographic Information Technology, Key Laboratory for Land Satellite Remote Sensing Applications of Ministry of Natural Resources, School of Geography and Ocean Science, Nanjing University, Nanjing, Jiangsu 210023, China

<sup>i</sup> Remote Sensing of Environmental Dynamics Laboratory, Department of Earth and Environmental Sciences (DISAT), University of Milano-Bicocca, Piazza della Scienza 1, Milano, Italy

<sup>j</sup> College of Agricultural, Consumer and Environmental Sciences, University of Illinois at Urbana Champaign, IL, USA

<sup>k</sup> National Center for Supercomputing Applications, University of Illinois at Urbana-Champaign, IL, USA

<sup>l</sup> Dynamic Meteorology Laboratory, Ecole Polytechnique, Palaiseau, France

<sup>m</sup> Department of Global Ecology, Carnegie Institution for Science, Stanford, CA, USA

<sup>n</sup> Jet Propulsion Laboratory, California Institute of Technology, Pasadena, CA, USA

## ARTICLE INFO

Editor: Jing M. Chen

## Keywords:

Sun-induced chlorophyll fluorescence

SIF

Photosynthesis

Near-infrared reflectance of vegetation

NIR<sub>v</sub>

Gross primary productivity

GPP

Remote sensing

## ABSTRACT

Sun-induced chlorophyll fluorescence (SIF) is a promising new tool for remotely estimating photosynthesis. However, the degree to which incoming solar radiation and the structure of the canopy rather than leaf physiology contribute to SIF variations is still not well characterized. Therefore, we investigated relationships between SIF and variables that at least partly capture the canopy structure component of SIF. For this, we relied on high-quality SIF observations from ground-based instruments, high-resolution airborne SIF imagery and the most recent satellite SIF products to cover large ranges in spatial and temporal resolution and diverse ecosystems. We found that the canopy structure-related near-infrared reflectance of vegetation multiplied by incoming sunlight (NIR<sub>v</sub>P) is a robust proxy for far-red SIF across a wide range of spatial and temporal scales. Our findings indicate that contributions from leaf physiology to SIF variability are small compared to the structure and radiation components. Also, NIR<sub>v</sub>P captured spatio-temporal patterns of canopy photosynthesis better than SIF, which seems to be mostly due to the greater retrieval noise of SIF. Compared to other relevant structural SIF proxies, NIR<sub>v</sub>P showed more robust relationships to SIF, especially at the global scale. Our results highlight the promise of using widely available NIR<sub>v</sub>P data for vegetation monitoring and also indicate the potential of using SIF and NIR<sub>v</sub>P in combination to extract physiological information from SIF.

## 1. Introduction

SIF is an electromagnetic signal emitted by chlorophyll *a* molecules when exposed to sunlight and is increasingly used for vegetation monitoring at regional and global scales (Frankenberg and Berry, 2018;

Mohammed et al., 2019; Ryu et al., 2019). SIF is a very weak signal compared to reflected sunlight as only a few percent of the absorbed energy is re-emitted as SIF (Frankenberg and Berry, 2018). This has important practical implications as the passive retrieval of SIF from the much stronger background signal can result in considerable retrieval

\* Corresponding author at: Department of Landscape Architecture and Rural Systems Engineering, Seoul National University, Seoul, South Korea.

E-mail address: [yryu@snu.ac.kr](mailto:yryu@snu.ac.kr) (Y. Ryu).

<https://doi.org/10.1016/j.rse.2021.112763>

Received 15 March 2021; Received in revised form 21 July 2021; Accepted 16 October 2021

Available online 12 November 2021

0034-4257/© 2021 The Authors. Published by Elsevier Inc. This is an open access article under the CC BY license (<http://creativecommons.org/licenses/by/4.0/>).

noise (Frankenberg and Berry, 2018; Joiner et al., 2020; Köhler et al., 2015). Along with the photochemical reflectance index (Gamon et al., 1992), SIF is rather unique among remote sensing indicators in being directly sensitive to changes in leaf photosynthetic physiology (Mohammed et al., 2019; Porcar-Castell et al., 2014). Applications of SIF are diverse including photosynthetic phenology (Guan et al., 2015; Walther et al., 2015), plant stress detection (Mohammed et al., 2019; Qiu et al., 2018), functional diversity (Tagliabue et al., 2020) and crop yield estimation (Guan et al., 2016; He et al., 2020; Peng et al., 2020), but the main goal of most SIF research is the remote estimation of terrestrial gross primary productivity (GPP) (Dechant et al., 2019; Migliavacca et al., 2017; Qiu et al., 2019; Ryu et al., 2019; K. Yang et al., 2018; Yang et al., 2015).

Canopy-level SIF is controlled by three main mechanistic factors, namely the light absorption (absorbed photosynthetically active radiation, APAR), chlorophyll fluorescence emission yield ( $\Phi_F$ ), and, in case of far-red SIF at about 760 nm, scattering of emitted fluorescence within the canopy that allows only a fraction of the emitted radiation to escape the canopy (Zeng et al., 2019) (canopy escape fraction,  $f_{esc}$ ; see Eq. (1) in Methods). While there is considerable knowledge about the dominant role of APAR as driver of SIF (Miao et al., 2018; Wieneke et al., 2018; K. Yang et al., 2018), the separate contributions from  $\Phi_F$  and  $f_{esc}$  to SIF observations are still not well characterized. Several experimental and modelling studies have reported that  $f_{esc}$  of far-red SIF can vary considerably over time and space due to changes in the canopy structure such as leaf area index, leaf angle distribution and clumping (Dechant et al., 2020; Qiu et al., 2019; Wang et al., 2020; Yang and van der Tol, 2018; Zeng et al., 2019). For  $\Phi_F$ , most work has been conducted at the leaf level. Although leaf-level  $\Phi_F$  responds to environmental stress (Flexas et al., 2002; Jonard et al., 2020; Mohammed et al., 2019),  $\Phi_F$  typically varies relatively little compared to the photochemical quantum yield of photosystem II ( $\Phi_{PSII}$ ) both at diurnal and seasonal time scales (Gu et al., 2019; van der Tol et al., 2014). Evergreen needleleaf forests are the exception to this pattern, with considerable seasonal  $\Phi_F$  variations due to physiological downregulation of photosynthesis during extended cold periods in winter (Magney et al., 2019; Porcar-Castell, 2011).

Based on current knowledge, canopy-level SIF variations are expected to be driven predominantly by APAR and  $f_{esc}$  rather than  $\Phi_F$ , at least in the absence of strong environmental stress and for ecosystems where  $fPAR$  and  $f_{esc}$  show important seasonal variations, i.e. excluding evergreen needleleaf forests. At sub-daily time scales, PAR is the dominant driver of SIF given the typically much smaller diurnal variations in the fraction of absorbed PAR ( $fPAR$ ),  $f_{esc}$  and  $\Phi_F$  (Chang et al., 2020; Dechant et al., 2020; Gu et al., 2019). At seasonal time scales, APAR and  $f_{esc}$  appear to show stronger variations compared to  $\Phi_F$  (Dechant et al., 2020; Wang et al., 2020). If indeed  $APAR \times f_{esc}$  is strongly correlated to SIF in most cases (see Eqs. (1)–(4) in the Methods section), it could be used as a structural proxy for SIF as recent studies have derived approaches to estimate  $fPAR \times f_{esc}$  from widely available reflectance observations (Yang et al., 2020; Zeng et al., 2019). In particular  $APAR \times f_{esc}$  can be approximated by  $NIR_{VP}$  (Dechant et al., 2020; Zeng et al., 2019), which is defined as the product of the near infrared reflectance of vegetation ( $NIR_V$ ) (Badgley et al., 2017) and incoming PAR (see Methods).

Despite recent findings on canopy structure effects and  $f_{esc}$  that seem to support the dominance of  $APAR \times f_{esc}$  in variations of SIF (Badgley et al., 2017; Dechant et al., 2020; Yang et al., 2020), a comprehensive evaluation to what degree  $NIR_{VP}$  and other related structural SIF proxies explain the variations of canopy SIF has not been reported. In particular, SIF is commonly compared to vegetation indices such as the enhanced vegetation index (EVI) (Huete et al., 2002) without considering PAR (Badgley et al., 2017; Li and Xiao, 2020; Qiu et al., 2020), which does not permit a meaningful direct comparison in cases where spatial and/or temporal variations of PAR are important. Furthermore, previous studies have not evaluated the spatial and temporal patterns of SIF and

$NIR_{VP}$  separately, but have instead focused either on long time and large spatial scales (Badgley et al., 2017) or examined only a few crop sites (Dechant et al., 2020; Yang et al., 2020).

Since one of the major goals of SIF research is to improve remote sensing based GPP estimation (Porcar-Castell et al., 2014; Ryu et al., 2019), it is important to also compare the performance of SIF and  $NIR_{VP}$  for this purpose. Several recent studies demonstrated the promise of using  $NIR_V$  and  $NIR_{VP}$  to estimate GPP across multiple spatial scales (Badgley et al., 2019; Badgley et al., 2017; Baldocchi et al., 2020; Jiang et al., 2020). However, direct comparisons of SIF and  $NIR_{VP}$  for GPP estimation using observations from the same sensors (or at least from the same viewing geometries) have been limited to a small set of crop sites (Dechant et al., 2020; Liu et al., 2020; Wu et al., 2019). When using observations from different satellites, differences in viewing geometry, overpass time and other factors related to data acquisition can affect results in addition to inherent differences between SIF and  $NIR_{VP}$ . Therefore, there is the need to directly compare SIF and  $NIR_{VP}$  regarding GPP estimation across different ecosystems at the site-level and, using the same satellite sensor for both variables, at the global scale.

In this study, we conducted i) a comprehensive evaluation of the relationship between  $NIR_{VP}$  and far-red SIF from plot to global scales and ii) a detailed direct comparison of far-red SIF and  $NIR_{VP}$  for GPP estimation with a strong focus on the global scale. We used a unique collection of observations that covers the majority of plant functional types and a wide range of temporal and spatial scales. In particular, this data collection includes observations from tower-based, airborne and satellite instruments with temporal resolutions ranging from half-hourly to monthly and spatial resolutions between 1 m and 50 km.

## 2. Materials and methods

### 2.1. Theoretical framework

Canopy-level far-red SIF, which we exclusively consider in this manuscript, can be decomposed into three mechanistic components, namely the absorbed fraction of photosynthetically active radiation (APAR), the canopy escape fraction, and the fluorescence emission yield,  $\Phi_F$  (Guanter et al., 2014):

$$SIF_{obs} = APAR \times f_{esc} \times \Phi_F \quad (1)$$

Our study relies on the previously established result (Zeng et al., 2019) that, except for very low fractional vegetation cover,  $f_{esc}$  for far-red SIF, which we exclusively consider in this manuscript, can be well approximated in the following way:

$$f_{esc} \approx \frac{NIR_V}{fPAR} \quad (2)$$

where  $fPAR$  is the fraction of photosynthetically active radiation absorbed and  $NIR_V$  is the near-infrared reflectance of vegetation estimated as  $NDVI \times NIR$  (Badgley et al., 2017), where  $NIR$  stands for near-infrared reflectance and  $NDVI$  is the Normalized Difference Vegetation Index (Rouse et al., 1974; Tucker, 1979). When substituting Eq. (2) into Eq. (1), using  $APAR = fPAR \times PAR$ , and using the definition.

$$NIR_{VP} = NIR_V \times PAR \quad (3)$$

we obtain the approximation.

$$SIF_{obs} \approx NIR_{VP} \times \Phi_F \quad (4)$$

which is the basis of our rationale that SIF, in terms of its variations, can be approximated by  $NIR_{VP}$  assuming relatively small variability of  $\Phi_F$  compared to the variability of  $NIR_{VP}$ . It is clear from Eq. (4) that  $\Phi_F$  can be estimated as the ratio of  $SIF/NIR_{VP}$  or as the slope in the linear regression of SIF vs.  $NIR_{VP}$ . Including an intercept term in the regression can account for either imperfect SIF retrieval (i.e. an offset), soil background impacts on  $NIR_{VP}$ , or both.

We use the convenient shorthand notation introduced in Eq. (3) also more generally for other vegetation indices (VI) that we consider potential structural SIF proxies in the way  $VIP = VI \times PAR$ . Thus, e.g. NDVI becomes NDVIP, which is also used for EVI2 (Jiang et al., 2008) and FCVI (Yang et al., 2020) and results in EVI2P and FCVIP as alternative structural SIF proxies.

## 2.2. Data sets and processing

### 2.2.1. Site data

We used previously published data from a total of six sites located in South Korea (rice) (K. Yang et al., 2018), China (corn 1) (Li et al., 2020), France (wheat) (Goulas et al., 2017), Spain (natural grassland) (Martini et al., 2019; Migliavacca et al., 2017; Zhang et al., 2020a) and the United States (corn 2 and soybean) (Wu et al., 2019). Only the rice paddy, corn 2 and soybean sites were irrigated/flooded. An overview of the site locations and key characteristics is shown in Table 1, Table S1 and Fig. S1. More details on the individual sites can be found in the corresponding references.

Tower-mounted spectrometers with sub-nanometer spectral resolution were used for SIF retrieval at all sites. These high-resolution spectrometers are combined with co-located lower-resolution spectrometers covering a larger spectral range, the visible and near-infrared (VNIR) range. Except for the wheat site that used the TriFLEX instrument (Daumard et al., 2010) and the grassland site which used a commercial FLoX instrument (JB Hyperspectral Devices, Düsseldorf, Germany) all other sites had set-ups similar to FluoSpec2 (X. Yang et al., 2018) based on the QEPro spectroradiometer (Ocean Optics, Dunedin, FL, USA), although with partly different spectral resolutions. An overview of all site-level and larger scale SIF datasets including information on the retrieval algorithm used is given in Table 1 below.

$NIR_V$  (Badgley et al., 2017) was calculated from the VNIR spectrometers and not from the instruments used for SIF retrieval for the following reasons. First, for some of the sites, the sensor used for SIF retrieval did not cover the red spectral band. Second, we did not observe disadvantages compared to using the same sensor as for SIF retrieval. NIR and red reflectance bands were calculated as averages of 600–650 nm and 800–850 nm, respectively, and used to calculate  $NIR_V$ , EVI2 (Jiang et al., 2008) and approximate FCVI (Yang et al., 2020) as the simple difference vegetation index NIR-red to ensure consistency with the airborne- and satellite-based results. Except for the rice paddy site which had a hemispheric viewing geometry for the upwelling radiation measurements, all other sites had a narrow angle field of view at nadir. PAR data was acquired with quantum sensors.  $NIR_V P$  was calculated as  $NIR_V \times PAR$ .

APAR was measured with either quantum (wheat, corn, soy) or LED (rice) sensors above and below the canopy at all sites except the grassland site. For the rice site, fPAR had to be gap-filled for part of the green-up period of the growing season using a radiative transfer model (Kim et al., 2019; K. Yang et al., 2018).

GPP was obtained via partitioning of net ecosystem exchange observations from eddy covariance measurements at all sites according to

the corresponding protocols. All GPP data was previously reported in publications. More details of the eddy covariance measurement and data processing methods are provided in Wu et al. (2019), Dechant et al. (2020) as well as the references in Table 1 and El-Madany (2018) for the grassland site. Negative GPP values were excluded from the analyses.

A Hampel outlier filtering (window length of 12 days, threshold parameter equals 3) was conducted for the grassland data to filter out strong outliers in the SIF time series. For all sites, data between 8 am and 4 pm local time were selected and negative SIF values were excluded as they were not available for most datasets. More details on methods and instrumentation can be found in the references given in Table 1.

To investigate if part of our results on the strong SIF-NIR<sub>V</sub>P relationship are consistent with the current theoretical understanding of SIF, we used simulations with the process-based model SCOPE (van der Tol et al., 2009; Vilfan et al., 2016) for the rice paddy site. To obtain a realistic scenario, the simulations were based on in-situ observations of meteorological conditions and relevant vegetation parameters in the rice paddy site. More details can be found in a previous publication from which the simulation outputs were reused here (Dechant et al., 2019).

### 2.2.2. Airborne data

We used data from the high-performance airborne imaging spectrometer HyPlant (Rascher et al., 2015; Siegmann et al., 2019). HyPlant consists of the FLUO module for SIF retrieval and the DUAL module for full-range reflectance. The FLUO sensor, which was specifically designed to be used for SIF retrieval (Rascher et al., 2015), covers the spectral range of 670–782 nm with a high spectral resolution of 0.3 nm (full width at half maximum) and has been used in the preparation for the upcoming FLEX satellite mission (Drusch et al., 2017). The VNIR sensor of the DUAL module we used covers the spectral range of 374–975 nm at a spectral resolution of 3.7 nm (full width at half maximum).

The crop dataset, on which we focused in our analysis, was acquired on June 29, 2018 at 12:30 CEST at 680 m above ground level in at the agricultural research station Campus Klein-Altendorf in western Germany (50.6167°N, 6.9833°E). More details can be found in the relevant references (Siegmann, 2019; Siegmann et al., 2019). We exclusively used original 1 m spatial resolution data in all analyses except Fig. S3d. The processing chain for the HyPlant data is describe in detail in Siegmann et al. (2019). Due to its robust performance, we chose the SIF retrievals based on the spectral fitting method (Meroni and Colombo, 2006; Siegmann et al., 2019).

$NIR_V P$  was estimated from FLUO at-sensor radiance data to ensure minimal differences compared to SIF retrievals in terms of sensor and processing aspects. The approach of using NIR radiance as proxy for the product of NIR reflectance times PAR was previously introduced as  $NIR_V R$  (Dechant et al., 2020) and was found to show good performance in terms of correlation to SIF and GPP at the site level (Dechant et al., 2020; Liu et al., 2020; Wu et al., 2019). Those results included observations in cloudy conditions where the largest differences between PAR and NIR radiance are expected, the discrepancies between the two variables should be even smaller in the clear sky conditions under which the airborne campaign was conducted.

**Table 1**

Overview of all SIF datasets used in this study. The location is given in units of degrees north (latitude) and east (longitude). The retrieval methods used include Singular Vector Decomposition (SVD), Spectral Fitting Method (SFM), improved Fraunhofer Line Depth (iFLD), and another version of FLD where 'n' indicates the number of channels used (nFLD).

Scale/platform	Vegetation type	Instrument	Retrieval method	Obs. geometry	Location (Lat./Long)	year	Literature reference
Tower	rice	Fluospec2	SVD	Hemispheric	38.2013/127.2506	2016	K. Yang et al. (2018)
	wheat	TriFLEX	nFLD	Nadir	43.9175/4.8797	2010	Goulas et al. (2017)
	corn (1)	Fluospec2	SFM	Nadir	34.5199/115.5916	2017	Li et al. (2020)
	corn (2)	Fluospec2	iFLD	Nadir	41.1649/−96.4701	2017	Wu et al. (2019)
	soybean	Fluospec2	iFLD	Nadir	41.1649/−96.4701	2018	Wu et al. (2019)
Airborne	grass	FLoX	SFM	Nadir	39.9403/−5.7639	2017	Migliavacca et al. (2017), Zhang et al. (2020a)
	crops	HyPlant	SFM	Nadir	50.6167/6.9833	2018	Siegmann (2019), Siegmann et al. (2019)
Satellite	All	TROPOMI	SVD	variable	All	2018	Köhler et al. (2018)

To ensure the smallest impact of the atmospheric path between the canopy and the sensor on our results, we chose the wavelengths for NIR as 756–758 nm, inside an atmospheric window (Guanter et al., 2013; Köhler et al., 2018). Although the NIR radiance at 756–758 nm also includes SIF, SIF contributes only several percent (Frankenberg and Berry, 2018) to the upwelling NIR radiance and therefore can be neglected for our purpose (see section 4.6). Red wavelengths were chosen in the range 670–684 nm in a compromise to average over a sufficiently large number of bands to increase signal quality but attempting to avoid atmospheric absorption features, especially the oxygen-B band, and shorter wavelengths which are more strongly affected by atmospheric scattering.

As no surface reflectance product was available for the FLUO data, we relied on the very strong linear relationships ( $R^2 > 0.99$ ) between DUAL at-sensor radiance and DUAL surface reflectance at the relevant wavelengths to convert FLUO at-sensor radiance data to FLUO surface reflectance for the calculation of NDVI, an estimate of FCVI via the difference vegetation index and EVI2. To do so, the linear regression coefficients obtained from the DUAL data were applied to the FLUO observations. To convert units of  $\text{mW m}^{-2} \text{sr}^{-1} \text{nm}^{-1}$  inherited from the radiance data to units of  $\text{nmol m}^{-2} \text{s}^{-1}$ , we used the very strong linear regression relationship ( $R^2 = 0.98$ ) between  $\text{NIR}_{\text{VP}}$  and  $\text{NIR}_{\text{VR}}$  at the site level.

Satellite data. We primarily used satellite SIF retrievals from the TROPOMI instrument on Sentinel-5P (Köhler et al., 2018). TROPOMI has an overpass time of 1:30 pm at the equator, a wide swath with viewing angles up to  $60^\circ$  that results in quasi-daily coverage of the earth's surface, and a revisit period of 17 days (Veefkind et al., 2012). The spatial resolution of TROPOMI in the year 2018 was equal or lower than  $7 \text{ km} \times 3.5\text{--}14 \text{ km}$  (depending on the view angle, Köhler et al., 2018). The spectral resolution of the near-infrared band 6 used both for the SIF retrieval and  $\text{NIR}_{\text{VP}}$  calculation is 0.38 nm (full width at half maximum).

The data-driven TROPOMI SIF retrieval method relies on a singular value decomposition of spectra in the range 743–758 nm over non-vegetated areas to derive spectral basis functions, which are subsequently used to model spectra including SIF (Köhler et al., 2018). The 2018 SIF and NIR radiance data was gridded to a  $0.05^\circ \times 0.05^\circ$  spatial resolution on a daily basis and then further aggregated to 8-day intervals.

For  $\text{NIR}_{\text{VP}}$ , we used an approach that is conceptually similar to the one we applied for the airborne data (i.e.  $\text{NIR}_{\text{VR}}$  (Dechant et al., 2020)). In particular,  $\text{NIR}_{\text{VP}}$  was estimated by multiplying the TROPOMI NIR radiance at 759 nm with MODIS NDVI, which was available at 0.05 degree resolution from the CMG product. MODIS rather than TROPOMI NDVI was used as no surface reflectance product is currently available for TROPOMI and the red band would have to be atmospherically corrected. MODIS NDVI was based on daily red and NIR nadir-adjusted surface reflectance products (MCD43D62, MCD43D63). Daily  $\text{NIR}_{\text{VP}}$  based on MODIS and TROPOMI was then aggregated to coarser temporal and spatial resolutions. The fixed value 0.1 was subtracted from NDVI to partially account for soil background (Badgley et al., 2017). Negative values of  $\text{NIR}_{\text{VP}}$  and  $\text{NIR}_{\text{V}}$  were excluded as they are typically caused by negative NDVI values related to snow. We used the TROPOMI NIR radiance at 759 nm, as it was provided in the original SIF data product and no atmospheric correction is necessary due to its location in an atmospheric window (Guanter et al., 2013; Köhler et al., 2018). This latter aspect ensures a direct comparability with the corresponding SIF retrievals as atmospheric correction for NIR at other wavelengths could introduce biases or artefacts leading to discrepancies between SIF and  $\text{NIR}_{\text{VP}}$ . As NIR radiance is very sensitive to clouds, we applied a cloud filtering. For this, we used the VIIRS-based cloud product (Siddans, 2017) with a threshold of 0.35 for the cloud fraction, which can reduce both direct cloud effects and indirect effects on the validity of using downwelling NIR radiance as a proxy for PAR. In addition to the cloud filtering, data with SIF signal uncertainty ( $1\text{-}\sigma$  retrieval error) larger

than  $0.55 \text{ mW m}^{-2} \text{sr}^{-1} \text{nm}^{-1}$  as well as SIF values  $>4$  or  $< -2 \text{ mW m}^{-2} \text{sr}^{-1} \text{nm}^{-1}$  were excluded from the analysis.

SIF and  $\text{NIR}_{\text{VP}}$  relationships were evaluated for instantaneous data, 8-day, 16-day and monthly composites. For evaluating results per PFT, we used the MODIS MCD12C1 land cover product. For the comparison of different variables to  $\text{NIR}_{\text{VP}}$  in terms of correlation to SIF, we relied on the same MODIS products as used for NDVI and multiplied the vegetation indices by BESS PAR (Ryu et al., 2018), which is also based on MODIS products. We approximated FCVI (Yang et al., 2020) by using the red band rather than the average of visible reflectance which is not available from MODIS. EVI2 was chosen rather than EVI as the blue band is sensitive to atmospheric correction errors and relying only on red and NIR bands permits a more direct comparison among the three indices ( $\text{NIR}_{\text{V}}$ , FCVI and EVI2) in terms of the equation used. Previous satellite-based results showing better performance of  $\text{NIR}_{\text{V}}$  compared to EVI (Duveiller et al., 2019) suggest that EVIP would not outperform  $\text{NIR}_{\text{VP}}$ . For  $\text{NIR}_{\text{VP}}$ , units of radiance were converted to PAR units in the same way as for the airborne data (see above). To evaluate the effect of PAR on the SIF- $\text{NIR}_{\text{VP}}$  relationship, we compared  $\text{NIR}_{\text{VP}}$  to  $\text{NIR}_{\text{V}}$ . Since no surface reflectance product is available for TROPOMI, we normalized at sensor NIR radiance by the cosine of the solar zenith angle following previous studies (Joiner et al., 2013). An overview of the different ways to calculate  $\text{NIR}_{\text{VP}}$  we used at the different scales is shown in Table S2.

As additional test, we compared MODIS  $\text{NIR}_{\text{VP}}$  with CSIF (Zhang et al., 2018), which is a machine learning product based on OCO-2 SIF retrievals, MODIS reflectance and fPAR products. Since the original version of the product did not cover 2018, we used the recently updated version 2 of the product. The CSIF data was available at  $0.05^\circ \times 0.05^\circ$  degree spatial and 4-day temporal resolution.

### 2.2.3. Global GPP

To evaluate the SIF-GPP relationship at the global scale, we used the ensemble RS + Meteo FLUXCOM GPP product (Jung et al., 2020; Jung et al., 2018), which uses machine learning algorithms to up-scale eddy covariance tower observations to the globe.

### 2.2.4. Analyses

For the slope analyses in SIF- $\text{NIR}_{\text{VP}}$ , and SIF-GPP as well as  $\text{NIR}_{\text{VP}}$ -GPP relationships, we conducted linear regression with either variable or constant intercept as there were artefacts for evergreen broadleaf forest due to the distribution of the data (only high values). The constant intercept was determined by averaging the median intercept in each PFT. For the case of temporal regression, evergreen broadleaf forest was excluded from the intercept calculation.

We relied on squared Pearson correlation as the main performance metric as it is equivalent to the coefficient of determination of linear regression with an intercept and a single explanatory variable.

### 2.2.5. Terminology

For the sake of simplicity, we refer to wavelengths within the spectral region of about 600–650 nm as 'red' and for wavelengths within the spectral region of the near-infrared plateau of about 750–900 nm as 'NIR'. This is also motivated by the relative stability of canopy reflectance in these regions. An overview of the exact spectral ranges used in the calculation of  $\text{NIR}_{\text{VP}}$  is shown in Table S2.

## 3. Results

### 3.1. Relationship between SIF and $\text{NIR}_{\text{VP}}$

#### 3.1.1. Tower-based measurements

At the site-level, we found very strong linear correlations between SIF and  $\text{NIR}_{\text{VP}}$  at the seasonal time scale (Fig. 1). The squared Pearson correlation ( $R^2$ ) between SIF and  $\text{NIR}_{\text{VP}}$  for individual sites ranged from 0.73 to 0.94 for half-hourly and 0.79 to 0.96 for daily data (Fig. S1a).  $\text{NIR}_{\text{VP}}$  performed slightly better than or similar to FCVIP and EVI2P (see

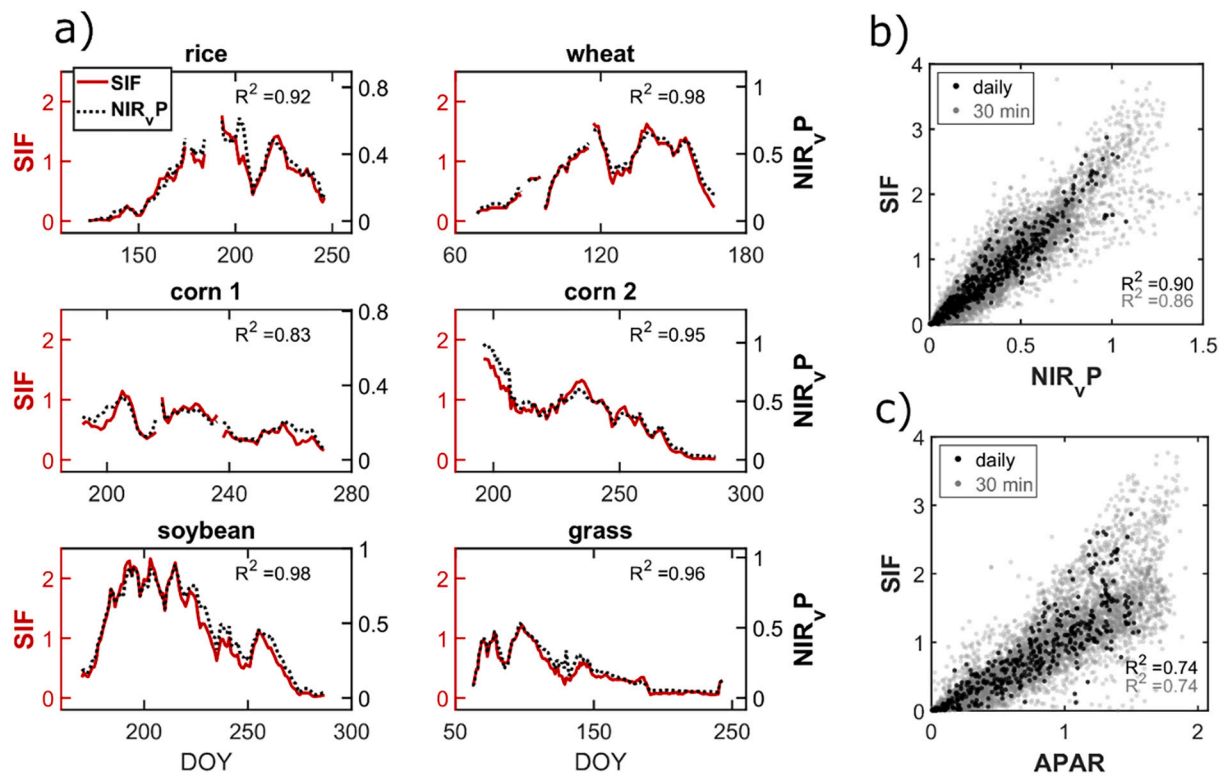


**Fig. 1.** Temporal dynamics of in-situ SIF and  $\text{NIR}_{\text{vP}}$  and their relationships. Data from six sites distributed in East Asia, Europe and North America are shown. a) Time series of 5-day moving average data are shown, DOY stands for day of the year. b), c) Scatterplot of half-hourly and daily data of SIF vs.  $\text{NIR}_{\text{vP}}$  or in-situ APAR for all site data combined. Note that for c) APAR was not available for the grassland site. SIF is given in units of  $\text{mW m}^{-2} \text{sr}^{-1} \text{nm}^{-1}$ ,  $\text{NIR}_{\text{vP}}$  and APAR in units of  $\text{nmol m}^{-2} \text{s}^{-1}$ .

Methods) for individual sites except for the two corn sites, where either FCVIP or EVI2P showed slightly stronger correlations (Fig. S3c).  $\text{NIR}_{\text{vP}}$  more clearly outperformed NDVIP, APAR and  $\text{NIR}_{\text{v}}$  alone (Fig. S2c). When combining the observations from all sites, the SIF- $\text{NIR}_{\text{vP}}$  correlation was high ( $R^2 = 0.86$  and  $0.90$  for half-hourly and daily data, respectively; Fig. 1b) and considerably stronger than the APAR- $\text{NIR}_{\text{vP}}$  correlation ( $R^2 = 0.74$  for both 30 min and daily data; Fig. 1c). The slopes of the SIF- $\text{NIR}_{\text{vP}}$  relationship differed somewhat between sites (Fig. S2a). Regarding the correlations of SIF and  $\text{NIR}_{\text{vP}}$  to GPP, two previous studies (Dechant et al., 2020; Wu et al., 2019) already reported higher or similar correlation of  $\text{NIR}_{\text{vP}}$  for the rice, wheat, soybean and the two corn datasets we used. In addition, we found that  $\text{NIR}_{\text{vP}}$  outperformed SIF also for the grassland site ( $R^2 = 0.60$  vs.  $0.49$  for half-hourly data; Fig. S2d).

### 3.1.2. Airborne measurements

At the landscape scale, the SIF- $\text{NIR}_{\text{vP}}$  relationship was predominantly linear for airborne SIF retrievals at 1 m resolution in a crop scene ( $R^2 = 0.86$ ) and  $\text{NIR}_{\text{vP}}$  captured SIF variations within and between larger crop fields well (Fig. 2a,c). Furthermore, the SIF- $\text{NIR}_{\text{vP}}$  relationship was strong and linear ( $R^2 = 0.89$ ) when selecting a subset of the flight line covering mostly small-scale plots where phenotyping experiments are performed and therefore larger variations in leaf physiology are expected (Fig. 2b,c). We observed a slight tendency towards saturation of  $\text{NIR}_{\text{vP}}$  at high SIF values (Fig. 2a,c).  $\text{NIR}_{\text{v}}$  had comparable correlation to SIF as FCVI, while EVI2 showed a slightly weaker correlation and NDVI showed strong saturation and only moderate correlation ( $R^2 = 0.63$ ; Fig. S3a,b).

### 3.1.3. Satellite observations

At the global scale, we found strong temporal correlations between SIF and  $\text{NIR}_{\text{vP}}$  (Fig. 3). The temporal SIF- $\text{NIR}_{\text{vP}}$  correlation of 8-day

composite data at 0.05 degree spatial resolution was very strong ( $R^2 > 0.80$ ) over large areas, especially in the northern hemisphere and for deciduous forests and crops (Figs. 3a). The temporal regression slopes showed spatial variations (Fig. S6a). When spatially averaging global data for each plant functional type (PFT), SIF and  $\text{NIR}_{\text{vP}}$  showed high temporal correlations, particularly for deciduous forests, evergreen needleleaf forests, crops and shrubland ( $R^2 \geq 0.9$ , Fig. 3b). For evergreen broadleaf forests, the correlation was lower ( $R^2 = 0.62$ ), but this was mostly due to the smaller seasonal variations of SIF which were well captured by  $\text{NIR}_{\text{vP}}$  both globally and in the Amazon (Fig. A1 in the Appendix).

Apart from the temporal correlations, we found strong spatial correlations between SIF and  $\text{NIR}_{\text{vP}}$  at the global scale ( $R^2 = 0.78$ , Fig. 4a, c). In particular,  $\text{NIR}_{\text{vP}}$  captured spatial SIF variations very well in North America where SIF shows very high values in the US Corn Belt ( $R^2 = 0.84$ , Fig. 4a,c) and the part of Eurasia that shows a band of high SIF values ( $R^2 = 0.77$ ; Fig. 4b,c). The spatial and spatio-temporal SIF- $\text{NIR}_{\text{vP}}$  correlations were high throughout the growing season in Europe, the US Corn Belt and globally (mostly  $R^2$  around 0.8 at 0.05 degree resolution; Fig. 5, Fig. S4), while monthly spatial correlations were somewhat lower for East Asia after the onset of the Monsoon (Fig. B1c, e). The spatial correlation for July and the spatio-temporal correlation of SIF vs.  $\text{NIR}_{\text{vP}}$  over the growing season showed indications of a weak nonlinearity towards high values at the global scale (Figs. 4c, 5c). Spatial regression slopes differed between PFTs and partly also showed considerable seasonal variations (Fig. S5, B1).

$\text{NIR}_{\text{vP}}$  had stronger spatial and temporal correlations with SIF than other variables that have previously been reported to be good SIF proxies such as APAR (K. Yang et al., 2018; Zhang et al., 2020b), EVI2P, and FCVIP (Yang et al., 2020) (Fig. C1). Both for TROPOMI SIF retrievals and SIF from the machine learning product CSIF (Zhang et al., 2018),  $\text{NIR}_{\text{vP}}$  had the highest spatial and temporal correlations to SIF followed

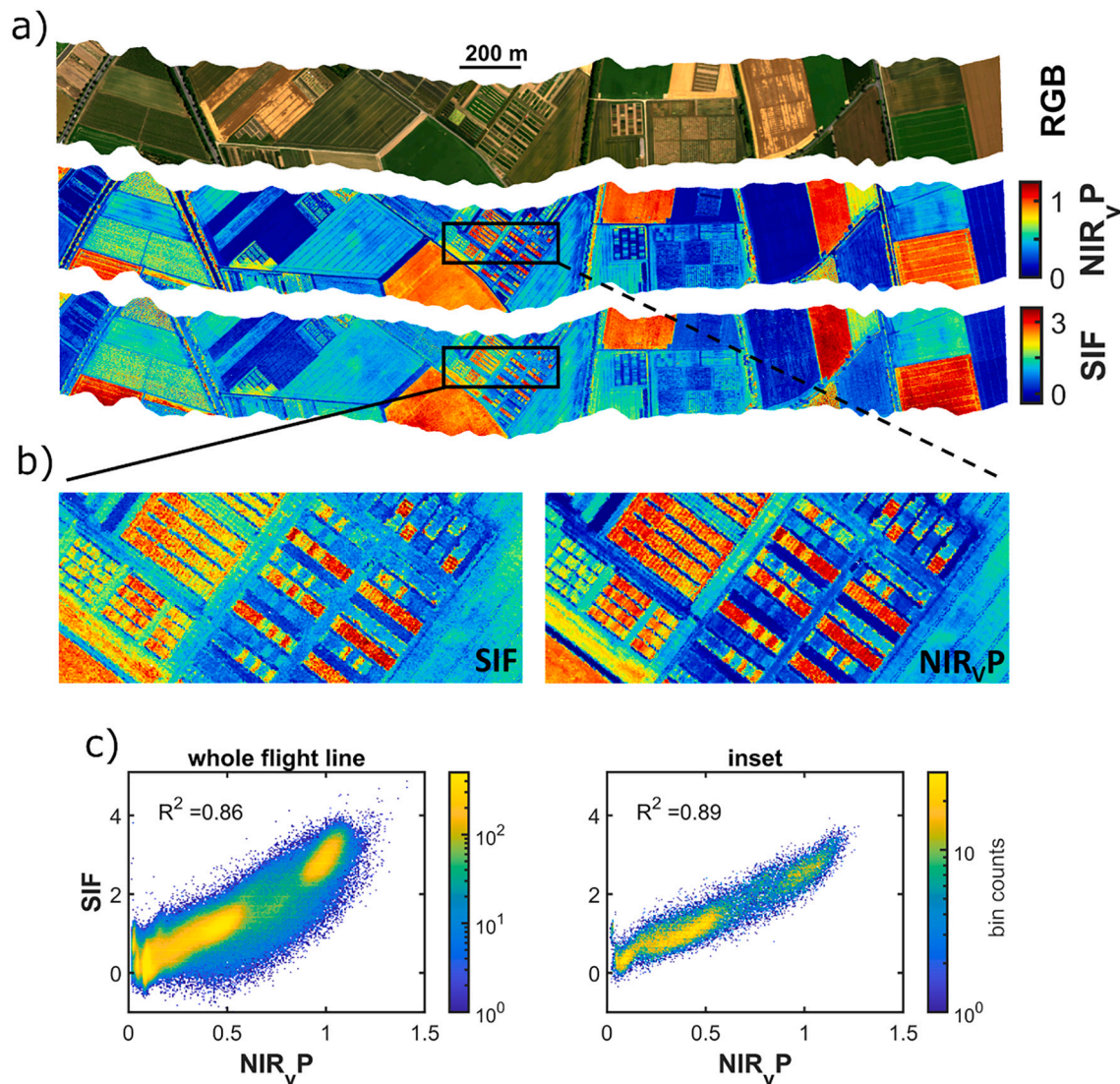


**Fig. 2.** Spatial patterns and relationships of airborne SIF and NIR<sub>v</sub>P observations over a crop landscape. Data was acquired with the HyPlant sensor over a crop landscape which is part of the agricultural research station Campus Klein-Altendorf, western Germany. All results are based on the original 1 m spatial resolution data. a) Entire flight lines of SIF, NIR<sub>v</sub>P and RGB composites, b) zoom to part of the flight line with small phenotyping plots, c) scatterplots corresponding to data shown in a) and b), the color scale indicates bin counts, i.e. point density. SIF is shown in units of  $\text{mW m}^{-2} \text{sr}^{-1} \text{nm}^{-1}$  and NIR<sub>v</sub>P in units of  $\text{nmol m}^{-2} \text{s}^{-1}$ .

by EVI2P, FCVIP, APAR and NDVIP (Fig. C1). The performance rankings were consistent for spatial and temporal correlations, but performance differences between structural SIF proxies were larger for the spatial correlation. APAR and NDVIP had comparable temporal correlations but showed differences for the spatial correlation.

### 3.2. Relationships to GPP

As SIF is commonly used as a proxy for GPP at large scales, we also evaluated the relationships of SIF and NIR<sub>v</sub>P to GPP both at the site level using tower-based data and at the global scale using TROPOMI-based SIF and NIR<sub>v</sub>P and FLUXCOM GPP (Jung et al., 2020; Jung et al., 2018) (see Methods).

#### 3.2.1. Site level

We found that NIR<sub>v</sub>P was strongly related to GPP at the six eddy covariance sites, with higher correlations between NIR<sub>v</sub>P and GPP than between SIF and GPP (Fig. 6). As C4 crops had considerably higher slopes in the SIF-GPP relationships than C3, we grouped the data according to photosynthetic pathway. When combining all data, NIR<sub>v</sub>P

showed somewhat different slopes for the two corn sites (Fig. S4) but when scaling NIR<sub>v</sub>P at each site with the slope from the corresponding SIF-NIR<sub>v</sub>P relationship, the higher NIR<sub>v</sub>P-GPP correlations can be well observed (Fig. 6a). In particular, NIR<sub>v</sub>P-GPP relationships showed a high degree of linearity for C3 and C4 crops while the SIF-GPP relationships showed saturation tendencies for both. When aggregating the time series from 30 min to daily and 3-day averages, correlations to GPP showed larger increases for SIF than for NIR<sub>v</sub>P, especially when going from half-hourly data to daily averages (Fig. 6b). The difference in median  $R^2$  between SIF-GPP and NIR<sub>v</sub>P-GPP gradually decreased with degree of temporal aggregation, from 0.13 at half-hourly time step over 0.07 at daily scale to zero at 3-day scale. However, even at 3-day scale NIR<sub>v</sub>P showed stronger correlations to GPP when taking into account the full distribution in  $R^2$  values, e.g. by comparing the lower quartiles. While the mean  $R^2$  values for the SIF-GPP relationship were not significantly lower than those of the NIR<sub>v</sub>P-GPP relationships at each aggregation level, for the half-hourly and the daily data the correlations to GPP were stronger for NIR<sub>v</sub>P than for SIF for each individual site.

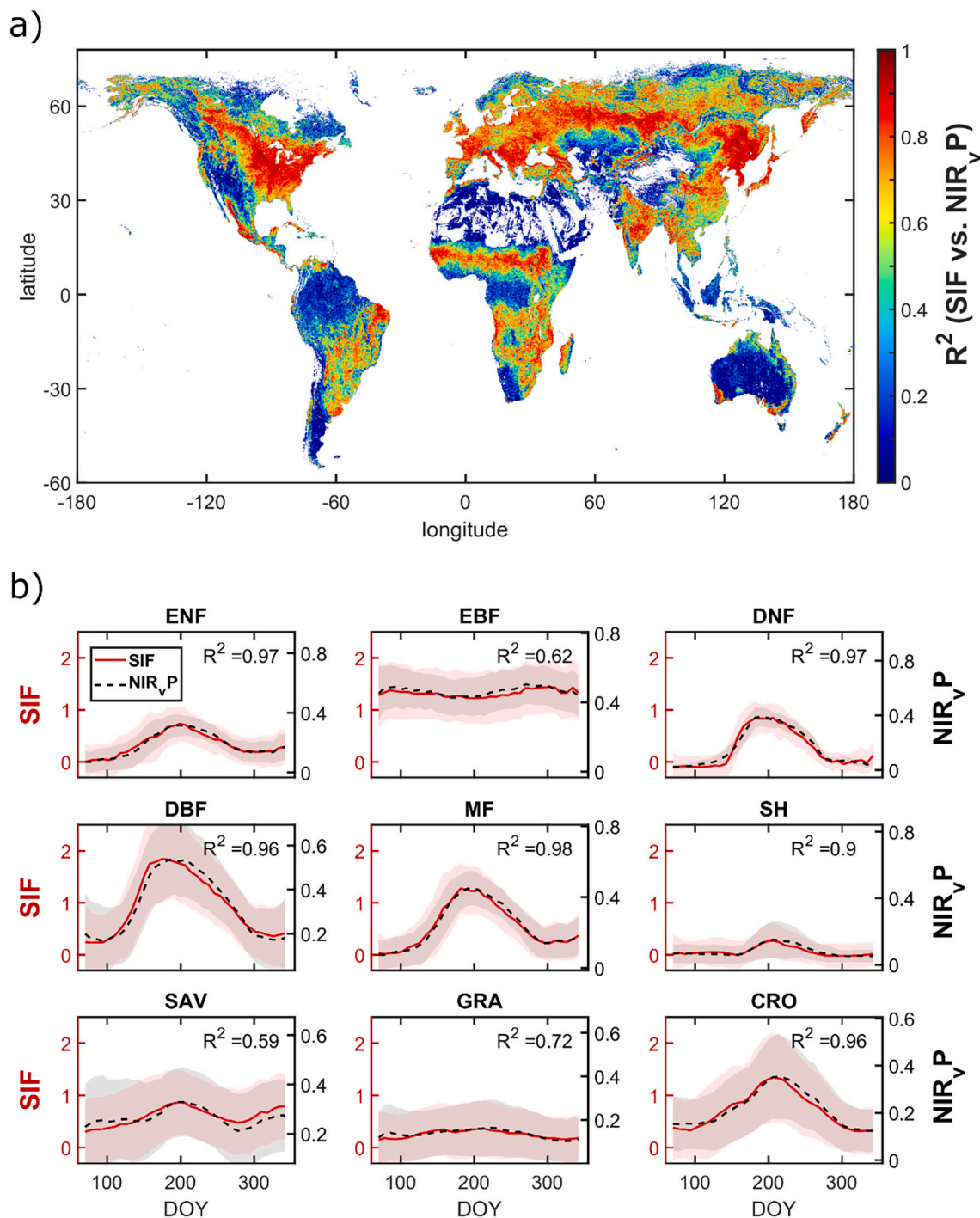


**Fig. 3.** Global-scale temporal dynamics and correlations of SIF and NIR<sub>v</sub>P. SIF retrievals and NIR<sub>v</sub>P based on the spaceborne TROPOMI instrument are shown for the year 2018. a) Per-pixel temporal correlation based on 8-day data at 0.05 degree spatial resolution. b) Mean SIF and NIR<sub>v</sub>P over all pixels for each plant functional type: evergreen needleleaf forest (ENF), evergreen broadleaf forest (EBF), deciduous needleleaf forest (DNF), deciduous broadleaf forest (DBF), mixed forest (MF), shrubland (SH), savanna (SAV), grassland (GRA) and cropland (CRO). The shading around the mean lines indicates one standard deviation. DOY stands for day of the year. SIF is shown in units of  $\text{mW m}^{-2} \text{sr}^{-1} \text{nm}^{-1}$  and NIR<sub>v</sub>P in units of  $\text{nmol m}^{-2} \text{s}^{-1}$ .

### 3.2.2. Global scale

We found that NIR<sub>v</sub>P was highly correlated to GPP and clearly outperformed SIF for both spatial, temporal and spatio-temporal correlations (Figs. 7, 8). The differences between the mean values of  $R^2$  for SIF-GPP and NIR<sub>v</sub>P vs. GPP were highly significant for both spatial and temporal correlations according to results from *t*-tests. Temporal aggregation led to larger increases in the correlation to GPP for SIF than for NIR<sub>v</sub>P (Fig. 8). This was apparent for both spatial and temporal

correlations but was more pronounced in the spatial case. The pattern of increasing correlation between SIF and GPP closely mirrors that of the corresponding SIF vs. NIR<sub>v</sub>P relationship, especially in the temporal domain (Fig. 8). The correlation and slopes for GPP relationships across PFTs were very similar for SIF and NIR<sub>v</sub>P (Figs. S3b,c; S8a) but the variability in slope was considerably larger for SIF than for NIR<sub>v</sub>P (Fig. S8b). NIR<sub>v</sub>P showed the strongest correlation to GPP among structural SIF proxies and the patterns of correlation strength to GPP were similar

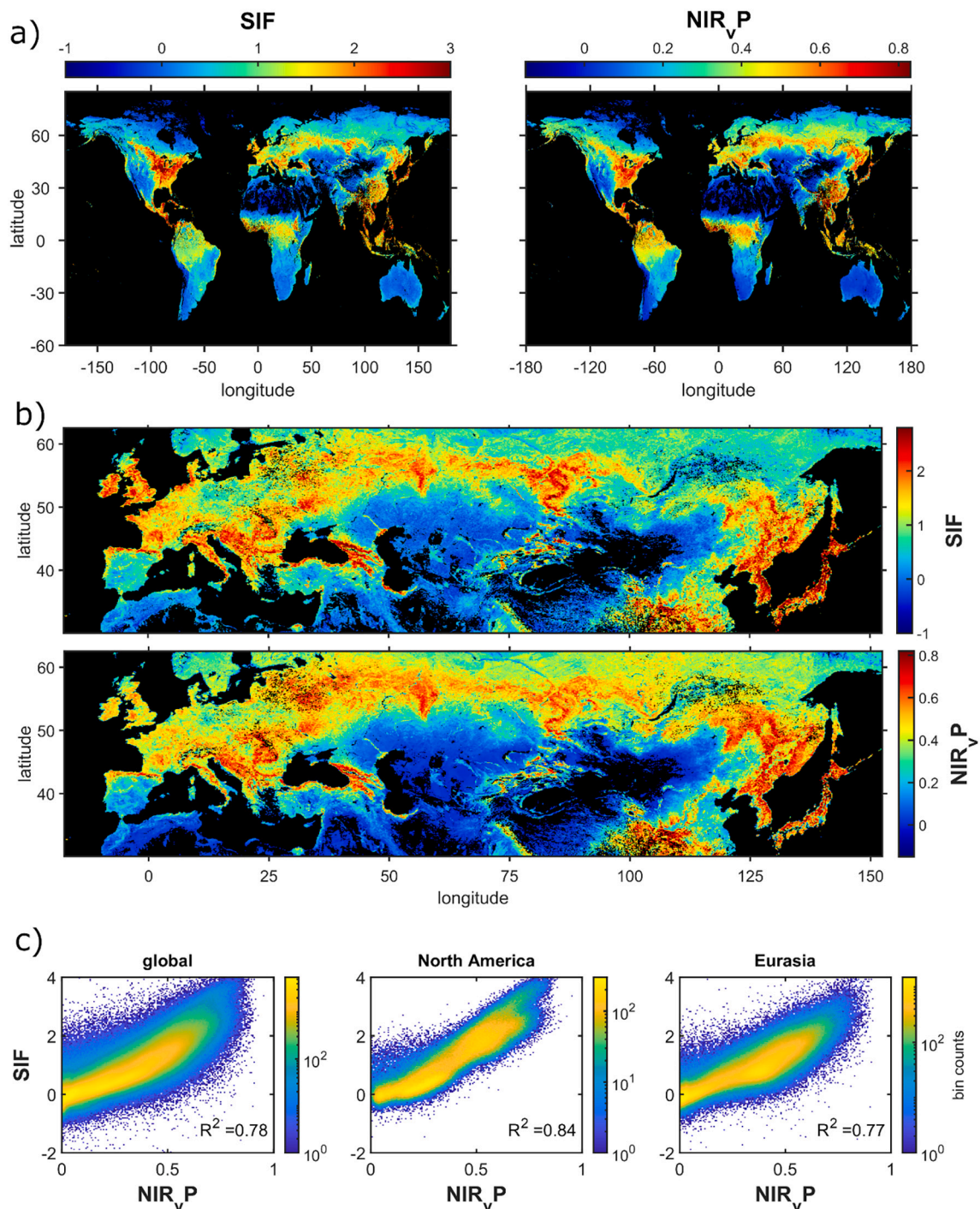


**Fig. 4.** Global-scale spatial patterns and relationships of SIF and NIR<sub>v</sub>P in July 2018. Data are from TROPOMI averaged over the month of July at a spatial resolution of 0.05 degree. a) Global maps and b) zoom on part of Eurasia with high SIF values, c) scatter plots of the global and Eurasia panels correspond to the maps shown in a) and c), while the North America panel is based on the geographical selection as in Fig. 5b; the color scale in c) indicates bin counts. SIF is shown in units of  $\text{mW m}^{-2} \text{sr}^{-1} \text{nm}^{-1}$  and NIR<sub>v</sub>P in units of  $\text{nmol m}^{-2} \text{s}^{-1}$ .

to those for SIF (Fig. C1).

## 4. Discussion

### 4.1. NIR<sub>v</sub>P as structural proxy for SIF

Overall, our analysis shows that NIR<sub>v</sub>P is a robust structural proxy for far-red SIF across ecosystems, spatial and temporal scales and instrument platforms (Figs. 1-5, Table 1). In particular, the SIF-NIR<sub>v</sub>P

relationship holds at very high spatial and temporal resolutions (Figs. 1 and 2), across different crop management regimes (e.g. irrigated vs. rainfed), at a Mediterranean grassland site that experiences very dry conditions (Fig. 1), and for a series of phenotyping plots where physiological variations are expected to be important (Fig. 2b,c).

Our results indicate that the physiological component in SIF, i.e. the  $\Phi_F$  term, varies little compared to the canopy structure and radiation component of SIF, i.e.  $\text{APAR} \times f_{\text{esc}}$ , and that this structural component is well captured by NIR<sub>v</sub>P (see Methods). More specifically,  $\Phi_F$  appears to

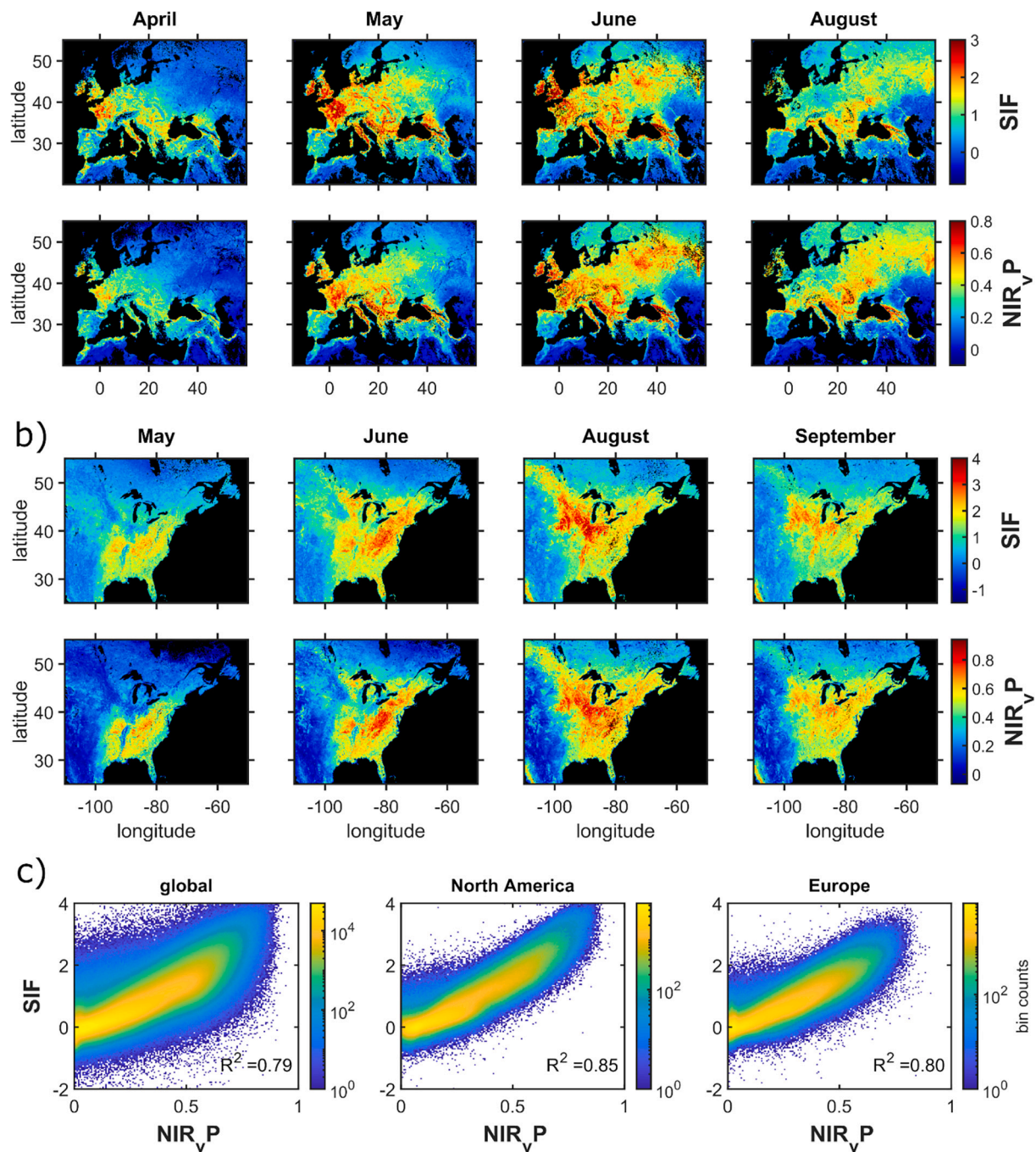


**Fig. 5.** Spatio-temporal patterns and relationships of SIF and NIR<sub>v</sub>P in Europe and North America. Monthly average TROPOMI data at 0.05 degree spatial resolution covering the main dynamics of the growing season. a) Europe and the b) North America focusing on the US Corn Belt, c) scatter plots based on monthly data for the main growing season from March to October. All data was evaluated at the spatial resolution of 0.05 degree. SIF is shown in units of  $\text{mW m}^{-2} \text{sr}^{-1} \text{nm}^{-1}$  and NIR<sub>v</sub>P in units of  $\text{nmol m}^{-2} \text{s}^{-1}$ .

not only vary considerably less than APAR, which has been previously established (Wieneke et al., 2018; K. Yang et al., 2018), but  $\Phi_F$  seems to also vary considerably less than  $f_{\text{esc}}$  (Fig. 1, Fig. S1) (Dechant et al., 2020; Wang et al., 2020). Therefore, ignoring variations in  $f_{\text{esc}}$  (Guanter et al., 2014) can lead to a misinterpretation of discrepancies between APAR and SIF (Dechant et al., 2020), as those discrepancies might be wrongly attributed to  $\Phi_F$ . Results from a process-based model (Fig. S9) further confirmed our observation-based findings and demonstrates that our interpretation of SIF being dominated by canopy structure and radiation is consistent with the current theoretical understanding of SIF (Gu et al., 2019; van der Tol et al., 2014) in addition to being supported

by empirical evidence from previous studies (Badgley et al., 2017; Dechant et al., 2020; Wang et al., 2020; Yang et al., 2020). The predominance of structure and radiation in explaining spatio-temporal variations of SIF in most ecosystems implies that many research applications that use SIF directly, i.e. without extracting or considerably enhancing its small physiological component, could instead use NIR<sub>v</sub>P without large reductions in performance, and potentially even some improvements (Peng et al., 2020).

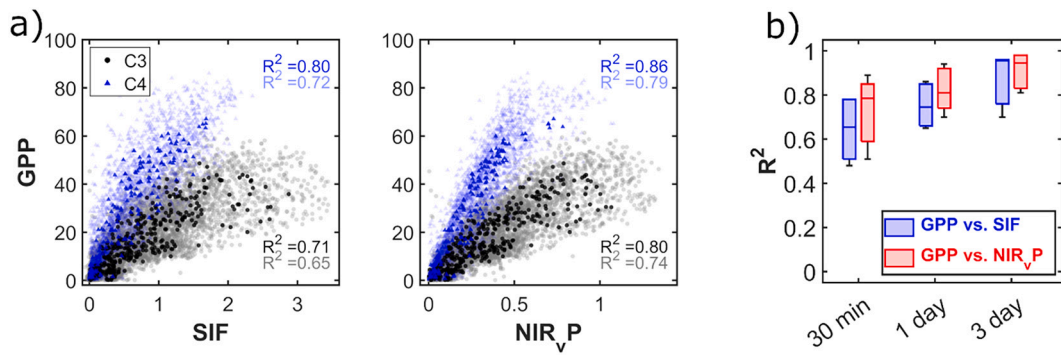


**Fig. 6.** Site-level relationships of SIF and NIR<sub>v</sub>P to GPP. SIF, NIR<sub>v</sub>P and GPP were measured at six eddy covariance towers including five crop sites (two C4, three C3) and one grassland site (same sites as in Fig. 1). a) Half-hourly relationships are shown in pale colors, daily average relationships in saturated colors. b) temporal aggregation effects on the relationships between SIF and GPP at individual sites. Data from all sites are combined and separated according to photosynthetic pathway C3 (black, filled circles) and C4 (blue, filled triangles). Note that for the sake of more direct visual comparability in a), NIR<sub>v</sub>P was adjusted for the slope in the SIF-NIR<sub>v</sub>P relationship for each site. GPP is given in units of  $\mu\text{mol m}^{-2} \text{s}^{-1}$ , SIF in  $\text{mW m}^{-2} \text{sr}^{-1} \text{nm}^{-1}$ , and NIR<sub>v</sub>P in  $\text{nmol m}^{-2} \text{s}^{-1}$ . (For interpretation of the references to color in this figure legend, the reader is referred to the web version of this article.)

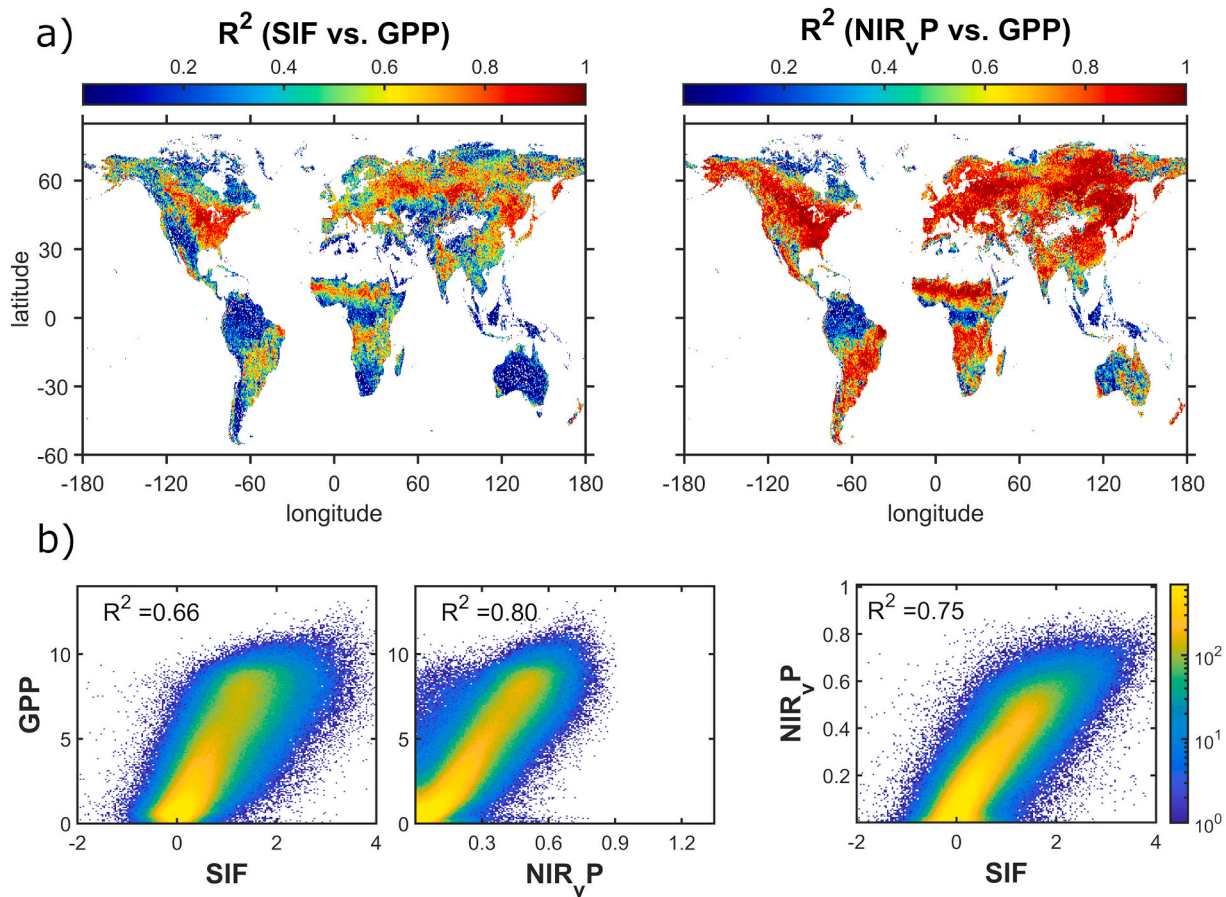


**Fig. 7.** Global-scale temporal and spatio-temporal correlations between SIF or NIR<sub>v</sub>P to GPP. SIF and NIR<sub>v</sub>P are based on TROPOMI and for GPP the FLUXCOM RS + METEO ensemble product was used. All results are based on data with 0.5 degree spatial and 8-day temporal resolution. a) temporal correlation maps, b) spatio-temporal correlations between either SIF, NIR<sub>v</sub>P and GPP for all available data in 2018; color in b) indicates point density (bin count). GPP is given in units of  $\text{gC m}^{-2} \text{d}^{-1}$ , SIF in  $\text{mW m}^{-2} \text{sr}^{-1} \text{nm}^{-1}$ , and NIR<sub>v</sub>P in  $\text{nmol m}^{-2} \text{s}^{-1}$ .

#### 4.2. NIR<sub>v</sub>P as structural proxy for GPP

We found that NIR<sub>v</sub>P is also a robust structural proxy for GPP at the site level and the global scale. Somewhat unexpectedly, NIR<sub>v</sub>P outperformed SIF not only at the site level, which was reported before (Dechant et al., 2020; Liu et al., 2020; Wu et al., 2019), but also in estimating global GPP at different spatio-temporal scales (Fig. 6, Fig.

S1d). From a theoretical standpoint, the shared structure and radiation components of SIF and NIR<sub>v</sub>P (Zeng et al., 2019), combined with relatively small variations in  $\Phi_F$  (Dechant et al., 2020), mean we should expect similar performance of SIF and NIR<sub>v</sub>P for GPP estimation supposing ideal, non-noisy signals. However, in contrast to NIR<sub>v</sub>P, which tends to have high signal quality, SIF is known to be affected by considerable retrieval noise (Frankenberg and Berry, 2018; Köhler et al.,

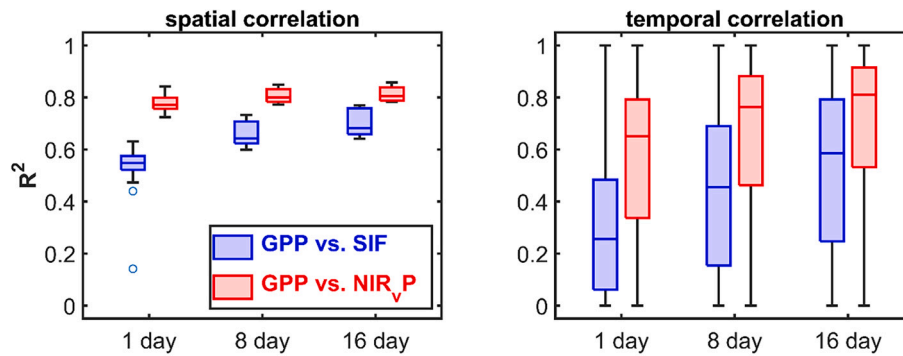


Fig. 8. Effect of temporal aggregation on global-scale temporal and spatial correlations between SIF or NIR<sub>v</sub>P to GPP. All data is the same as in Fig. 7 except for the temporal resolution as indicated on the x-axis. Results for SIF vs. NIR<sub>v</sub>P are shown for reference.

2015) (Table 2).

Several aspects of our results support the interpretation that differences in signal quality might explain the weaker GPP estimation performance of SIF compared to NIR<sub>v</sub>P. First, the temporal aggregation results (Figs. 6b, 8, Fig. S4) suggest that SIF suffers from considerable noise while NIR<sub>v</sub>P and GPP both have much higher signal quality. Noise is reduced with temporal aggregation and correlation strength is expected to considerably increase as a consequence, which matches the observed patterns of correlations involving SIF. For the correlation between NIR<sub>v</sub>P and GPP, however, the increase with temporal aggregation was much less pronounced, especially for the global-scale spatial correlation. Second, the close relationship between PFT-level patterns of slopes and correlation in the SIF-GPP and NIR<sub>v</sub>P-GPP relationships indicate strong similarities between SIF and NIR<sub>v</sub>P despite the differences in overall correlation (Figs. S3b, S8a). In our findings, only the much larger coefficient of variation in the SIF-GPP slopes compared to the NIR<sub>v</sub>P-GPP slopes aggregated to PFT level (Fig. S8b) cannot be easily explained by invoking SIF retrieval noise and therefore other potential reasons for these differences should be investigated.

At the site level, we found that when combining data from all sites there were considerable differences in the slopes of the SIF-GPP and NIR<sub>v</sub>P-GPP relationships between C3 and C4 crops. These differences are known from previous studies (e.g. Dechant et al., 2020; Zhang et al., 2020a) and are mainly due to the higher GPP in C4 crops for a given APAR value as C4 photosynthesis is more efficient due to the absence of photorespiration. While for SIF and NIR<sub>v</sub>P, contributions from  $\Phi_F$  and  $f_{esc}$  could affect the C3 vs. C4 slope differences, previous studies did not find indications of clearly different  $\Phi_F$  or  $f_{esc}$  for C4 compared to C3 crops (Dechant et al., 2020; Wang et al., 2020). Therefore, the relative slope differences between C3 and C4 crops are expected to be similar for SIF, NIR<sub>v</sub>P and APAR.

In contrast to the expectation of similar slope differences motivated above, we found that the slopes in the NIR<sub>v</sub>P-GPP relationships differed considerably for the two corn sites (Fig. S4) while they were rather similar for the corresponding SIF-GPP relationships (Fig. 6a). This can be attributed to the different slopes in the corresponding SIF-NIR<sub>v</sub>P relationships, where corn 1 (China, rainfed) showed the highest and corn 2 (US, irrigated) the lowest of all slopes (Fig. S2). Such large differences are unexpected, especially for the same crop type as the theory implies that, apart from uncertainties introduced by approximating the product  $fPAR \times f_{esc}$  with NIR<sub>v</sub>, the only factor that affects the slopes is  $\Phi_F$ .  $\Phi_F$  magnitude at a given APAR is known to respond mostly to  $V_{cmax}$  (Camino et al., 2019; Lee et al., 2015; Zhang et al., 2014) and it appears unlikely that the corn 1 site has a 1.78 times higher  $V_{cmax}$  compared to corn 2. Wu et al. (2019) reported overall similar slope values for three different corn site-years with only slightly higher slopes in case of the irrigated compared to the rainfed fields while in our case the rainfed field showed the much higher slope. Liu et al. (2020) reported relatively similar slope values as Wu et al. (2019) although with some variation between years which was also reported by Baldocchi et al. (2020) but in no case could we find slope differences of similar magnitude as we observed. Therefore, we suspect a bias either in SIF magnitude and/or in reflectance calibration in one of the two corn sites we used. As we could not identify the origin of the bias, we chose to report the relationships between scaled, i.e. slope-adjusted NIR<sub>v</sub>P and GPP in Fig. 6 as this permits the most direct comparison to the SIF-GPP relationship. Effectively, we used NIR<sub>v</sub>P as a SIF proxy in this case as we applied the linear regression model for SIF based on NIR<sub>v</sub>P as predictor. In this case, the focus is then on the variability around the regression slopes, which shows considerably more linear and stronger scaled NIR<sub>v</sub>P-GPP than SIF-GPP relationships (Fig. 6a). We believe that more work is needed to investigate slope differences in SIF-GPP compared to NIR<sub>v</sub>P-GPP

Table 2

Comparison of strengths and weaknesses of SIF and NIR<sub>v</sub>P. The comparison addresses important aspects related either to data acquisition, quality and availability, or application for vegetation monitoring. + indicates an advantage, - a disadvantage and the number of + symbols provide a rough indication of the relative advantage over the other variable. ‘Ease of measurement’ refers to required complexity and performance levels of instruments as well as their cost, ‘data availability’ focusses on long-term data with high spatio-temporal resolution; ‘signal quality’ refers to the signal-to-noise-ratio of currently available satellite products; ‘background signals’ stand for non-vegetated surfaces such as soil, or impervious surfaces in urban areas; ‘vegetation structural information’ refers to canopy structure characteristics such as leaf area index, clumping and leaf inclination angle, ‘vegetation physiological information’ refers to signals related to dynamic changes in leaf photosynthetic activity.

	Ease of measurement	Data availability	Signal quality	Insensitivity to clouds	Insensitivity to background signals (soil)	Vegetation structural information	Vegetation physiological information
SIF	-	-	-	+	++	++	++
NIR <sub>v</sub> P	++	++	++	-	+	++	-

relationships across sites and years. Ideally, such studies should make use of standardized sensors, calibration methods and retrieval algorithms.

Our results on the direct comparison of SIF and NIR<sub>v</sub>P for GPP estimation confirm and considerably extend previous findings from site-level studies on crops (Dechant et al., 2020; Liu et al., 2020; Wu et al., 2019). Apart from the novel global-scale results, we also extended the site-level analyses. First, we analyzed six different sites located distributed globally in the northern hemisphere in a combined way. Second, we confirmed that previous site-level results showing better GPP estimation performance of NIR<sub>v</sub>P compared to SIF in crops (Dechant et al., 2020; Liu et al., 2020; Wu et al., 2019) also held in a Mediterranean grassland site which experiences drought (Fig. S2d). NIR<sub>v</sub>P is expected to not fully capture physiological responses of photosynthetic light use efficiency to short-term drought and heat stress in crops and natural ecosystems as well as the photosynthetic downregulation in evergreen needleleaf forests in winter, since in both cases canopy structure is relatively stable (Dechant et al., 2020; Magney et al., 2019). However, in both cases canopy structure was found to play an important role for GPP estimation. Xu et al. (2021) conducted a water stress experiment in potato and found that the stress response of SIF was caused both by changes in leaf physiology and leaf angles as captured by  $\Phi_F$  and  $f_{esc}$ , respectively. Kim et al. (2021) reported that, despite its small seasonal variation, canopy structure as captured by  $f_{esc}$  partly tracked changes in photosynthetic light use efficiency during the fall transition in a temperate evergreen needleleaf forest site. In particular,  $f_{esc}$  better captured the response of photosynthetic light use efficiency to diffuse radiation than  $\Phi_F$ . Further research is needed to examine if these findings also hold at other sites.

#### 4.3. Differences between NIR<sub>v</sub>P and SIF

Despite the robust SIF-NIR<sub>v</sub>P correlation across a wide range of spatial and temporal scales, we found differences between the two variables. Conceptually, such differences could be due to differences in data acquisition and processing of SIF and NIR<sub>v</sub>P, e.g. due to the use of different sensors, limitations in signal quality of either variable, limitations of NIR<sub>v</sub>P as an approximation of the structure and radiation component of SIF, or the physiological variations in SIF which are not captured by NIR<sub>v</sub>P. We tried to minimize differences in data acquisition and processing by using observations from the same sensors and found that this clearly improved the SIF-NIR<sub>v</sub>P relationship for airborne and satellite data (Fig. S3b, S7). Several of our results indicate that the lower signal quality of SIF is an important factor explaining observed differences between SIF and NIR<sub>v</sub>P. In addition to the GPP estimation results discussed above (esp. Figs. 6, 8b), relevant results regarding the retrieval noise in SIF include higher correlations of NIR<sub>v</sub>P to enhanced machine learning based SIF products compared to original SIF retrievals (Fig. C1b) and extremely strong and linear SIF-NIR<sub>v</sub>P relationships based on simulated, noise-free data (Fig. S9). Apart from the SIF retrieval noise, we found a strong effect of clouds on the SIF-NIR<sub>v</sub>P relationship and despite a rather strict filtering (see Methods) cloud contamination still affected the results, especially for East Asia during the monsoon period that starts in July (Fig. B1a) and the tropics (Fig. S5). A stricter filtering would have limited the data availability for our analysis.

Setting aside discrepancies between SIF and NIR<sub>v</sub>P related to signal quality or the use of different sensors, we found some indications of a slight saturation of NIR<sub>v</sub>P at high values of SIF for spatial and spatio-temporal relationships (Figs. 2c, 4c, 5c). However, the apparently similar saturation patterns seem to be due to different factors for the airborne and satellite data. For the airborne data, the saturation of NIR<sub>v</sub>P appears to be inherited from NDVI (Fig. S3c), which might indicate limitations of NIR<sub>v</sub>P to capture the APAR  $\times$   $f_{esc}$  component of SIF. For the satellite data, in contrast, we found a saturation in spatial and spatio-temporal SIF-NIR<sub>v</sub>P relationships only for the global scale

when combining all data (Figs. 4c, 5c), but not for large regions such as North America, Europe and Eurasia or data grouped by PFT (Figs. 4c, 5c, Fig. S7). This suggests that saturation at the global scale results from differences in the SIF-NIR<sub>v</sub>P slope across regions, e.g. North America vs. Eurasia (Figs. 4c, 5c), which, when data are combined can cause apparent saturation. The slope differences between large geographical regions such as North America vs. Europe are likely caused by different fractional coverage in terms of PFTs, as slopes differed between PFTs (Fig. S5) but differences in seasonal slope variation for a given PFT might also contribute. The saturation effects for both the airborne and satellite data were clearly reduced when aggregating to coarser spatial scales (Figs. S2d; S3 center panel vs. Fig. 5c left hand panel) and the spatio-temporal, global-scale saturation was not consistently apparent in all months (Fig. B1d). It should also be mentioned that the high level of spatial aggregation appears to partly explain the difference between low or moderate pixel-level (Fig. S3b) and very high PFT-level SIF-NIR<sub>v</sub>P correlations (Fig. 3b), especially for evergreen needleleaf forests where stronger differences are expected based on known physiological mechanisms (Magney et al., 2019; Porcar-Castell, 2011). Therefore, detailed analyses at finer spatial scales are needed. Such studies should consider using enhanced SIF products with higher signal quality and spatio-temporal resolution (Wen et al., 2020; Zhang et al., 2018) or higher quality SIF retrievals that will be available in the future from new satellites (Drusch et al., 2017; Mohammed et al., 2019). Regarding the patterns of higher and lower temporal SIF-NIR<sub>v</sub>P correlations within PFTs (Fig. 3a, Fig. S5b), the degree of seasonality can at least partly explain this: EBF, SHR and GRA have the lowest levels of correlation and also have the lowest seasonal variabilities (Fig. 3b).

#### 4.4. Variations in the physiological component of SIF

The variation of regression slopes between SIF and NIR<sub>v</sub>P deserves special consideration as it is theoretically related to variations in  $\Phi_F$  (see Methods, Eq. (4)). We observed considerable spatial and temporal variations of SIF-NIR<sub>v</sub>P regression slopes at large scales (Figs. S4, S3, S7). When aggregated to the level of PFTs, the regression slopes partly agree with spatial variations in photosynthetic capacity,  $V_{cmax}$ , especially when using a fixed intercept (Fig. D1). This is consistent with the known sensitivity of SIF and  $\Phi_F$  to  $V_{cmax}$  (Camino et al., 2019; Lee et al., 2015; Zhang et al., 2014) and indicates the potential usefulness of combining SIF and NIR<sub>v</sub>P to extract  $\Phi_F$ . In contrast to the global scale, the variations in regression slopes at the site level (Fig. S2a) could mostly be caused by differences in instruments and SIF retrieval methods (see Table 1 in the Methods section) which are known to considerably affect SIF magnitude (Chang et al., 2020). In the spatial domain, similar regression analyses as for the temporal domain could be conducted but we chose to use the simpler approximation by calculating the ratio of SIF/NIR<sub>v</sub>P instead as regression intercepts tended to vary relatively little and for the airborne data the regression approach is not applicable. At the global scale, we observed considerable temporal variations of the PFT-level SIF/NIR<sub>v</sub>P ratio (Fig. 9) that appear to be meaningful in terms of seasonal leaf dynamics of leaf physiology. Interestingly, the temporal variations of SIF/NIR<sub>v</sub>P seem to peak earlier in the growing season compared to previously reported temporal variations of chlorophyll content (Croft et al., 2020) which is also known to covary with photosynthetic capacity (Croft et al., 2016). This apparent discrepancy in seasonal dynamics of different remotely sensing-based proxies of  $V_{cmax}$  will require further evaluation, ideally on the basis of ground observations. At the landscape scale, we found considerable differences in the SIF/NIR<sub>v</sub>P ratio between crop fields based on the high-resolution airborne data (Fig. S3e) that might reflect differences in leaf physiology. Although our results appear promising regarding  $\Phi_F$  estimation and its potential for vegetation monitoring, further detailed investigation will be necessary to evaluate the quality of  $\Phi_F$  estimates and better understand its variations regarding physiological mechanisms.

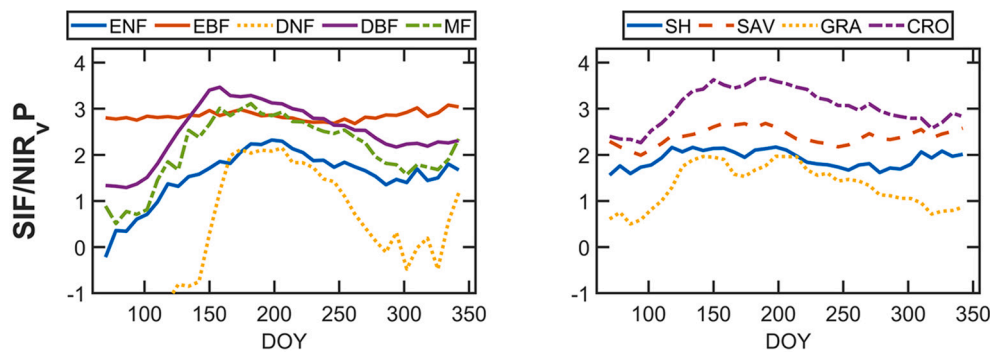


**Fig. 9.** Temporal dynamics of the ratio of SIF to  $\text{NIR}_{\text{vP}}$  for different ecosystems. The results shown on are based on 8-day TROPOMI data at 0.05 degree spatial resolution as Fig. 3b. The abbreviations of the plant functional types are: evergreen needleleaf forest (ENF), evergreen broadleaf forest (EBF), deciduous needleleaf forest (DNF), deciduous broadleaf forest (DBF), mixed forest (MF), shrubland (SH), savanna (SAV), grassland (GRA) and cropland (CRO).

#### 4.5. $\text{NIR}_{\text{vP}}$ compared to other structural SIF proxies

We found that, overall,  $\text{NIR}_{\text{vP}}$  showed stronger correlations to SIF compared to the other structural SIF proxies (Figs. S1c, S2a, S7a). In particular, the consistently lower SIF-APAR correlations compared to SIF- $\text{NIR}_{\text{vP}}$  correlations indicates an important role of  $f_{\text{esc}}$ . At the site level, we used total APAR rather than the so called green APAR, which is the actually relevant part for SIF. However, this can unlikely explain the large differences in seasonal dynamics of APAR compared to SIF (Fig. S2b) as the differences between green and total APAR are expected to be strongest in the senescence phase of crops (Gitelson and Gamon, 2015).

Regarding the better performance of  $\text{NIR}_{\text{vP}}$  compared to FCVIP and EVI2P, we found relatively small differences at the site level and for the airborne data (Figs. S1d, S2a). However, we found that EVI2P and especially FCVIP are more strongly affected by soil background in very sparse vegetation. This effect could be partly seen from site-level results where the difference to  $\text{NIR}_{\text{vP}}$  was largest for the grassland site (Fig. S1c), which has low LAI for a considerable part of the year, but was most apparent at the global scale where soil background characteristics are most variable (Fig. C1a).

Despite its better performance compared to other structural SIF proxies,  $\text{NIR}_{\text{vP}}$  is still affected by soil background signals for very sparse vegetation which, together with lower SIF signal quality, could potentially explain lower SIF- $\text{NIR}_{\text{vP}}$  temporal correlations in shrublands, savanna and grassland ecosystems (Fig. 2a, Fig. S3a). Some straightforward practical strategies to further reduce the soil background signal in  $\text{NIR}_{\text{vP}}$  have already been proposed recently (Jiang et al., 2020; Zeng et al., 2019). However, although simple and robust, the NDVI-based approach to estimating the near-infrared reflectance of vegetation is limited both in terms of the degree of soil background suppression and the selection of the chlorophyll-related, ‘green’ vegetation signal. To overcome these limitations, more refined approaches could be developed that might make use of hyperspectral observations to better separate the soil and (green) vegetation signals.

$\text{NIR}_{\text{v}}$  alone, i.e. without taking PAR into account, showed strong performance at the global scale (Fig. C1b), but more detailed analyses revealed that  $\text{NIR}_{\text{v}}$  considerably overestimates SIF in fall when vegetation is still green but PAR decreases (Fig. A1b). These findings indicate a clear advantage of  $\text{NIR}_{\text{vP}}$  over  $\text{NIR}_{\text{v}}$  even at longer time scales (e.g. weekly to monthly) due to seasonal variations of PAR. It should be noted, however, that the better performance of  $\text{NIR}_{\text{vP}}$  compared to  $\text{NIR}_{\text{v}}$  for satellite snapshot observations may not be apparent when comparing data from different satellites due to differences in overpass times and, potentially, observation geometry that affects the atmospheric transmission of upwelling light to the sensor (Fig. C1b). Differences between  $\text{NIR}_{\text{vP}}$  and  $\text{NIR}_{\text{v}}$  regarding their correlation to SIF and GPP are expected

to become more important when using data from upcoming geostationary satellite missions such as GeoCarb, TEMPO and Sentinel-4 (Mohammed et al., 2019). As canopy-level PAR cannot be directly observed from airplanes or satellites, either a simple approach that approximates PAR via the downwelling NIR radiance (Baldochi et al., 2020; Dechant et al., 2020; Wu et al., 2019), or more complex methods involving atmospheric radiative transfer modelling (Jiang et al., 2020; Ryu et al., 2018) or machine learning (Hao et al., 2019) can be used. The radiance-based approach has previously been shown to have comparable performance with direct PAR observations at the site level (Dechant et al., 2020).

#### 4.6. Sources of uncertainty and limitations

Regarding the site-level data, different instruments and algorithms were used to retrieve SIF and measure  $\text{NIR}_{\text{vP}}$ . This could affect both the level of noise in the SIF retrievals as well as the overall magnitude (Dechant et al., 2020), which might be one reason for differences in the slopes between SIF and  $\text{NIR}_{\text{vP}}$  (Fig. S3). Another factor can be the reflectance calibration, that could affect the magnitude of  $\text{NIR}_{\text{vP}}$  and hence the SIF- $\text{NIR}_{\text{vP}}$  and GPP-  $\text{NIR}_{\text{vP}}$  slopes (Fig. S4).

For the airborne data, some uncertainty could be introduced by our approach to transfer atmospheric correction information from the lower resolution DUAL data to the high spectral resolution FLUO data (see Methods). The impact of this is expected to be limited, however, as the area imaged was relatively small and the sky was clear during the flight.

In the processing of  $\text{NIR}_{\text{vP}}$  based on satellite data, we had to combine data from two sensors on different satellites as for the TROPOMI instrument no surface reflectance data product is available. This approach is not commonly used and could introduce uncertainties as the viewing geometries and overpass times of MODIS and TROPOMI are not the same. However, it is well known that NDVI is much less sensitive to viewing geometry and overpass time effects than, for example, NIR reflectance, as some of the effects cancel out when taking the ratios of reflectance or their differences (Sims et al., 2011; Tucker et al., 2000; Verrelst et al., 2008). Another relevant aspect is that the NIR wavelengths of MODIS and TROPOMI are not the same, which means that three different wavelengths are involved. This, however, does not have a large impact on  $\text{NIR}_{\text{vP}}$  as the sensitivity of  $\text{NIR}_{\text{vP}}$  to the choice of NIR wavelength for NDVI or the NIR factor is low (Fig. S10). For the reasons mentioned above, we think our approach is robust although it would be preferable to use data from a single instrument. Regarding the main conclusions of our study, it should be noted that any discrepancies between the MODIS NDVI we used and the NDVI using TROPOMI sensor and acquisition characteristics would lead to a decrease in the correlation between SIF and  $\text{NIR}_{\text{vP}}$ .

Regarding the calculation of  $\text{NIR}_{\text{VP}}$  from the HyPlant FLUO and TROPOMI sensors, we used NIR wavelengths around 759 nm where atmospheric effects can be neglected at the high spectral resolution of the corresponding sensors. This is conceptually suboptimal when trying to compare SIF from an entirely independent version of  $\text{NIR}_{\text{VP}}$  as, technically speaking,  $\text{NIR}_{\text{VP}}$  in this wavelength range is based on the apparent reflectance that contains small contributions related to the SIF emission. However, using radiative transfer simulations, we could demonstrate that the contribution from SIF to  $\text{NIR}_{\text{VP}}$  in this case is small enough to ignore and, in particular, cannot explain the strong relationship between SIF and  $\text{NIR}_{\text{VP}}$  (Fig. S10). While it would be preferable to use NIR wavelengths above 800 nm in the calculation of  $\text{NIR}_{\text{VP}}$  as we have done for the site-level data, this requires a sensor that covers this spectral range and an atmospherically corrected reflectance product.

For the sake of greater consistency across scales, we approximated FCVI by the simple difference vegetation index  $\text{NIR} - \text{red}$ . This differs from the original definition of FCVI where the average of the whole visible range is subtracted from NIR but we found that the effects of our approximations are small and do not affect the correlations between FCVI and SIF much at the site level (Fig. S10b). Therefore, we think the approximation is valid and does not affect the airborne- and satellite-based results much either.

Overall, we acknowledge that we had to use different ways to calculate  $\text{NIR}_{\text{VP}}$  and other structural SIF proxies such as FVIP and EVI2P at the different scales (Table S2) but we think our conclusions are still valid as the sensitivities of these variables to the exact choice of wavelengths in the red and NIR spectral regions is low (Fig. S10).

We are aware that the magnitudes of SIF and  $\text{NIR}_{\text{VP}}$  appear to differ somewhat between the different scales. This can be due to different reasons including different SIF retrieval algorithms (Chang et al., 2020; Marrs et al., 2021; Siegmann et al., 2019), calibration biases, overpass times of the satellite as well as effects of viewing geometry. This, however, does not affect the validity of our analyses and conclusions as we did not use data from different scales in combined analyses. The Pearson correlation metric on which we strongly relied is insensitive to magnitude bias effects and the variations of slopes between SIF,  $\text{NIR}_{\text{VP}}$  and GPP were only considered in a relative sense for a given scale. Previous studies have demonstrated that SIF can be retrieved with consistent magnitudes when using consistent retrieval algorithms and similar instrument characteristics (e.g. Magney et al., 2019; Sun et al., 2017).

#### 4.7. Complementarity of SIF and $\text{NIR}_{\text{VP}}$

All evidence indicates that SIF and  $\text{NIR}_{\text{VP}}$  are complementary measurements. SIF offers two distinct advantages for improved vegetation monitoring. First, the characteristics of its emission and retrieval make SIF insensitive to soil (emission) and less sensitive to thin clouds (retrieval) than the reflectance or radiance measurements involved in  $\text{NIR}_{\text{VP}}$  (Turner et al., 2019) (Table 2). Second, SIF contains unique physiological information in the form of  $\Phi_F$  (Magney et al., 2019; Porcar-Castell et al., 2014, p.).  $\Phi_F$  is thought to explain the faster and stronger stress response of SIF compared to structural variables such as APAR, NDVI or EVI (and, in all likelihood, also  $\text{NIR}_{\text{VP}}$ ) as observed in extreme events such as drought or heat waves (Jonard et al., 2020; Li and Xiao, 2020; Qiu et al., 2020; Wieneke et al., 2018; Wohlfahrt et al., 2018). However, these apparent advantages of SIF can be offset by considerable practical limitations in terms of data availability, spatio-temporal resolution and signal quality (Peng et al., 2020; Ryu et al., 2019; Somkuti et al., 2020) (Figs. 6-8).  $\text{NIR}_{\text{VP}}$ , in contrast, has long term data records (Badgley et al., 2019) with high signal quality and, increasingly, very high spatio-temporal resolution (Badgley et al., 2017; Jiang et al., 2020) (Table 2) and therefore has advantages over SIF with respect to its structure and radiation component.

Apart from the individual advantages of SIF and  $\text{NIR}_{\text{VP}}$ , they can be effectively used in combination for at least two purposes. First, the ratio  $\text{SIF}/\text{NIR}_{\text{VP}}$  or the corresponding regression slope can be used to estimate

the physiological component of SIF,  $\Phi_F$  (Dechant et al., 2020) (see Methods and Figs. S3d, S10). As  $\Phi_F$  estimation amplifies SIF retrieval noise (Dechant et al., 2020), however, very high quality SIF products should be used to avoid the need for aggregation to coarser scales. Second, since SIF and  $\text{NIR}_{\text{VP}}$  share the same structure and radiation components ( $\text{APAR} \times f_{\text{esc}}$ ) and  $\text{NIR}_{\text{VP}}$  typically has higher signal quality than SIF, evaluating the SIF- $\text{NIR}_{\text{VP}}$  relationship can be used to assess the quality of SIF retrievals beyond diurnal variations that are strongly driven by PAR (Chang et al., 2020).  $\text{NIR}_{\text{VP}}$  might therefore prove helpful in further improving SIF retrieval methods as they continue to be refined (Chang et al., 2020; Cogliati et al., 2019; Siegmann, 2019).

## 5. Conclusion

We comprehensively evaluated the relationships between SIF and  $\text{NIR}_{\text{VP}}$  across a wide range of spatial and temporal scales using a unique combination of in-situ, airborne and satellite datasets. We found that the SIF- $\text{NIR}_{\text{VP}}$  relationship is strong and robust across spatio-temporal scales ranging from 30 min to one month and from 1 m to 50 km. Moreover, the  $\text{NIR}_{\text{VP}}$  was more strongly related to SIF than other relevant structural SIF proxies. In particular, the SIF- $\text{NIR}_{\text{VP}}$  relationship was considerably stronger than the SIF-APAR relationship indicating an important role of the escape fraction  $f_{\text{esc}}$ , i.e. canopy scattering. Although the SIF- $\text{NIR}_{\text{VP}}$  relationship was strong and consistent across scales, we found clear indications of spatio-temporal variations of the SIF- $\text{NIR}_{\text{VP}}$  slope, which is an estimate of the physiological emission yield  $\Phi_F$ . These slope variations appear to be related to  $V_{\text{cmax}}$  and also seem to at least partly explain a weak non-linearity of the SIF- $\text{NIR}_{\text{VP}}$  relationship in the spatial dimension. Further detailed study of spatial and temporal patterns of  $\Phi_F$  is needed, as well as the potential discrepancies of SIF and  $\text{NIR}_{\text{VP}}$  under environmental stress conditions. Regarding the highly relevant application of GPP estimation, we found that  $\text{NIR}_{\text{VP}}$  can be used as a structural proxy for SIF to estimate GPP both in natural ecosystems and crops. In fact,  $\text{NIR}_{\text{VP}}$  was even more strongly related to global FLUXCOM GPP than TROPOMI SIF, which appears to be mostly due to noise in the SIF retrievals.

Overall, our study demonstrates the importance of canopy structure and solar radiation for understanding variations of SIF and GPP over a large range of spatio-temporal scales. We therefore expect  $\text{NIR}_{\text{VP}}$ , which can capture most of these variations, to be more widely applied in future research on remote estimation of GPP, crop yield modelling and other related subjects. Furthermore, making more effective use of the physiological information in SIF by extracting it with the help of  $\text{NIR}_{\text{VP}}$  might result in improved GPP estimation and new insights on vegetation dynamics.

## Data and code availability

Site data is available from the respective site PIs upon request. The airborne HyPlant dataset is available for download (<https://doi.ipk-gatersleben.de/DOI/3dede5ba-d57a-4cf5-9d06-6fd9a70f52c9/d5a1e61e-b0c7-447b-81f5-d94ffad7dc0c/2>). TROPOMI SIF retrieval products are also available for download (<ftp://fluo.gps.caltech.edu/data/tropomi/>). MODIS data can be downloaded from NASA. CSIF is also available for download (<https://figshare.com/articles/CSIF/6387494>). Custom code for data processing and analysis is available from the authors upon request.

## Declaration of Competing Interest

The authors declare that they have no known competing financial interests or personal relationships that could have appeared to influence the work reported in this paper.

**Acknowledgements**

This study was funded by National Research Foundation of Korea (NRF-2019R1A2C2084626). We thank a large number of colleagues for contributing to the site datasets as well as the airborne and satellite SIF products. For the site-level SIF and NIR<sub>v</sub> measurements, we would like to acknowledge the support from Kaige Yang, Jongmin Kim, Genghong Wu, Guofang Miao, Hyungsuk Kim, Zhaohui Li, Qian Zhang, Fabrice Daumard, and David Martini. We also thank many colleagues for providing the site-level GPP data, in particular, Minseok Kang, Andy Suyker, Guofang Miao, Ji Li, Hezhou Wang, Tarek El-Madany, and Olivier Marloie. We are also grateful for the contributions of Chongya

Jiang to the BESS modelling platform and thank Yulin Yan, Seungjoon Lee, Bolun Li, and Juwon Kong for downloading and processing MODIS data. We thank Bastian Siegmann for providing useful information and additional data related to the HyPlant dataset. Furthermore, we thank Martin Jung and Ulrich Weber for sharing the FLUXCOM products and Yao Zhang and Pierre Gentine for making the CSIF dataset publicly available. We also thank three anonymous reviewers for providing comments that helped improve the manuscript. This work is a contribution to the LEMONTREE (Land Ecosystem Models based On New Theory, obseRvations and ExperimEnts) project, funded through the generosity of Eric and Wendy Schmidt by recommendation of the Schmidt Futures program (YR).

**Appendix A. Temporal patterns of SIF and NIR<sub>v</sub>P at large scales**

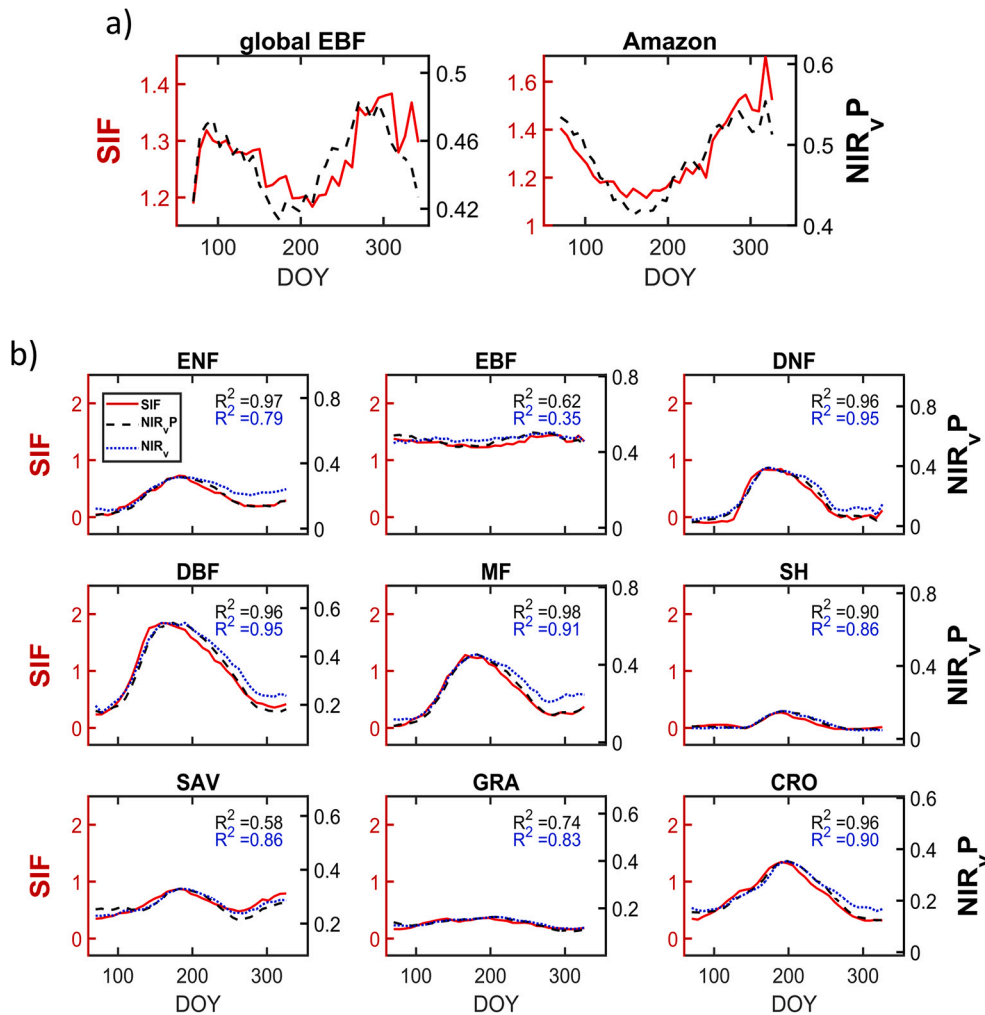


**Fig. A1.** Additional results for SIF-NIR<sub>v</sub>P temporal relationships. Correlation based on 8-daily, 0.05 degree TROPOMI data for different plant functional types (PFTs). Results shown here complement main Fig. 2. a) detail of seasonal patterns of SIF (red line) and NIR<sub>v</sub>P (black dashed line) in the tropics, either for all EBF, combined, or separately for the Amazon basin, b) direct comparison of NIR<sub>v</sub>P vs. NIR<sub>v</sub> (see Methods); NIR<sub>v</sub> is shown in relative units. SIF is shown in units of mW m<sup>-2</sup> sr<sup>-1</sup> nm<sup>-1</sup>, and NIR<sub>v</sub>P in nmol m<sup>-2</sup> s<sup>-1</sup>. (For interpretation of the references to color in this figure legend, the reader is referred to the web version of this article.)

Appendix B. Temporal variation of SIF- NIR<sub>v</sub>P slopes and spatio-temporal patterns in East Asia

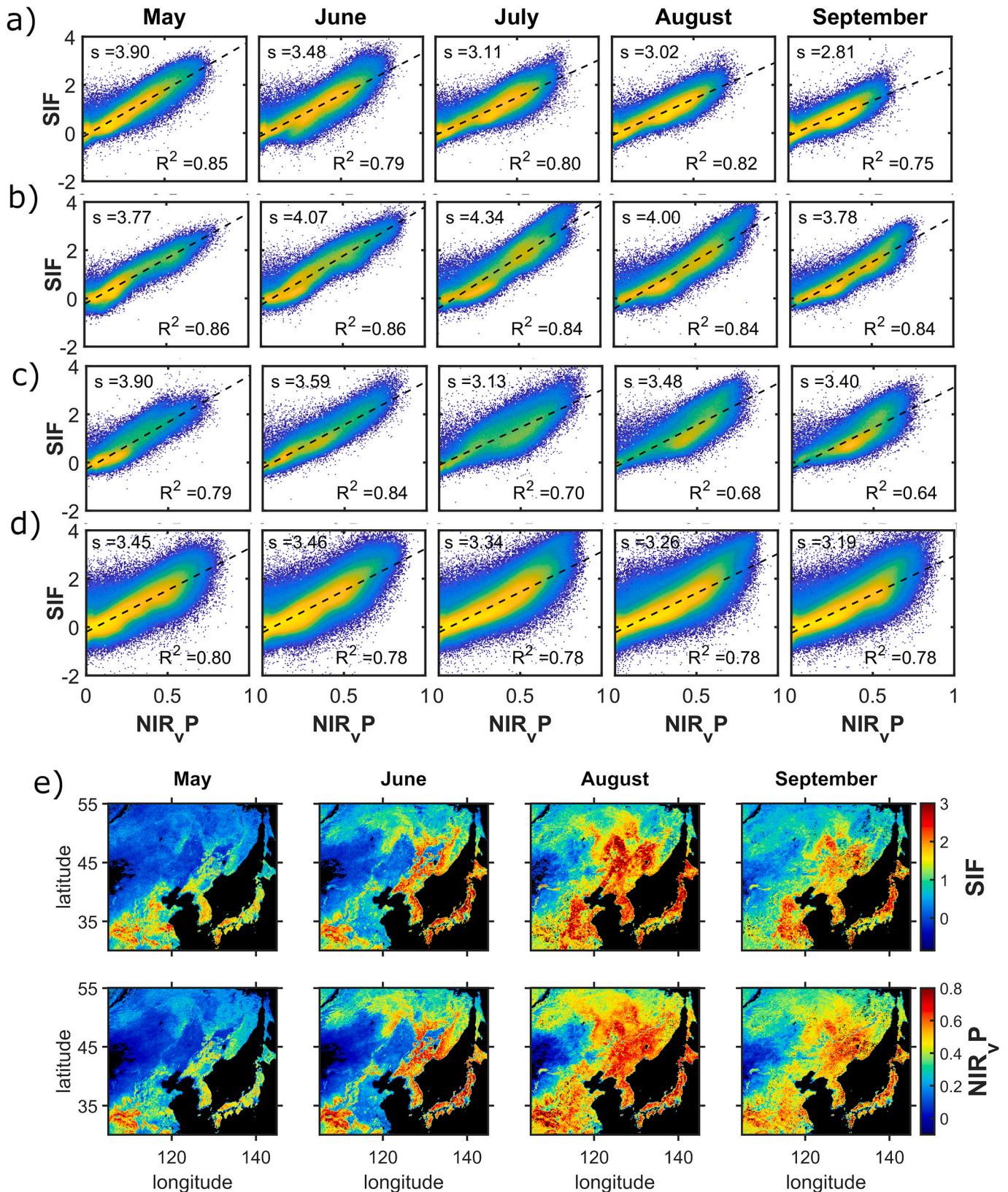


**Fig. B1.** Additional detailed results for the spatial relationships between SIF and NIR<sub>v</sub>P across the growing season. Results are shown for a) Europe, b) North America, c) East Asia, and d) the whole globe. Results are complementary to Fig. 5a,b. ‘s’ indicates the linear regression slope. SIF is shown in units of  $\text{mW m}^{-2} \text{sr}^{-1} \text{nm}^{-1}$  and NIR<sub>v</sub>P in units of  $\text{nmol m}^{-2} \text{s}^{-1}$ . The plot for Europe in April is not shown for reasons of consistency across regions, the corresponding statistical results for Europe in April were:  $R^2 = 0.81$ ,  $s = 4.13$ . In d) the monthly maps are shown for the East Asia region selected for the scatterplots in c). In a)-d), color indicates point density (brighter colors have higher densities).

Appendix C. Comparison of different structural SIF proxies at the global scale

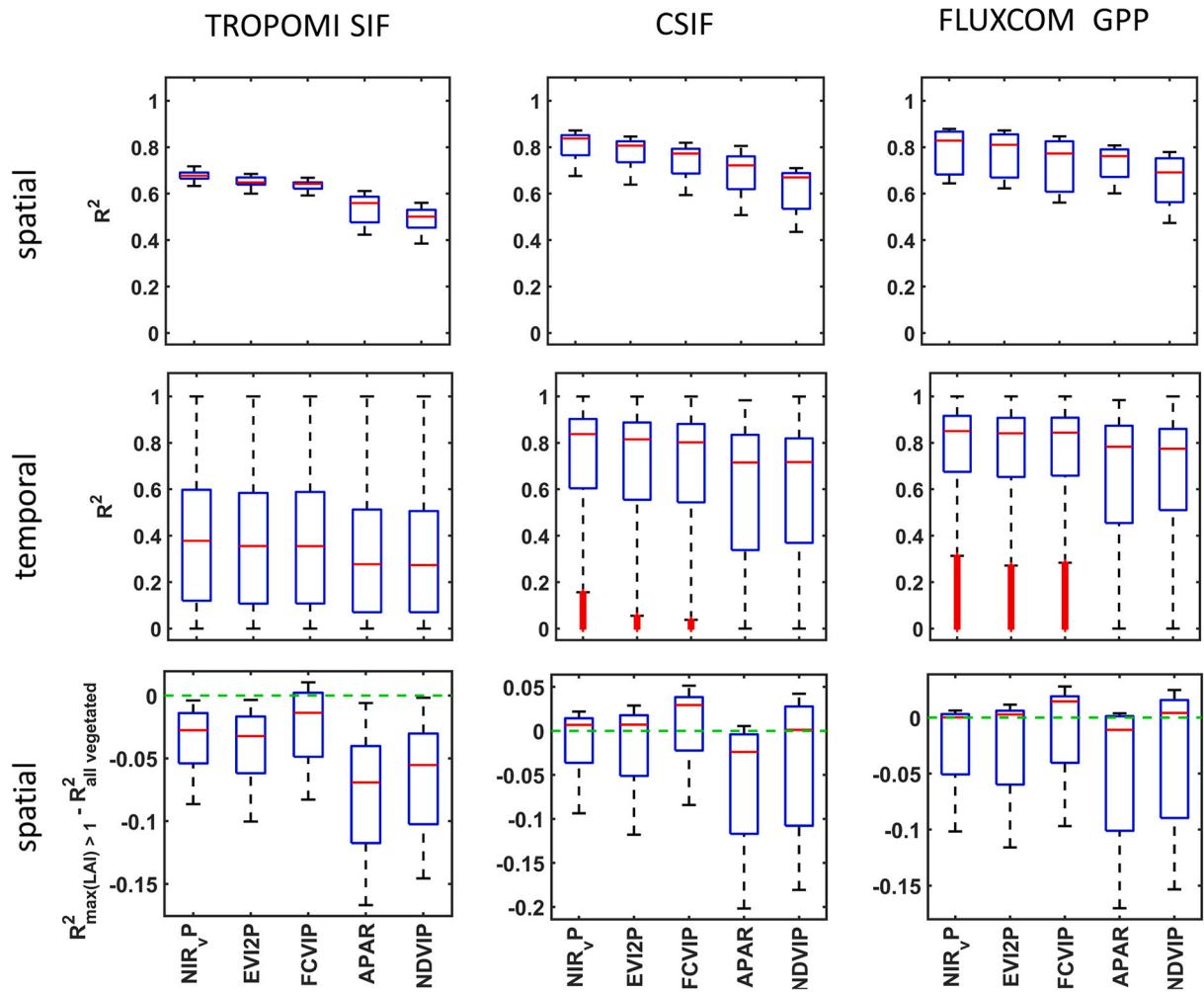
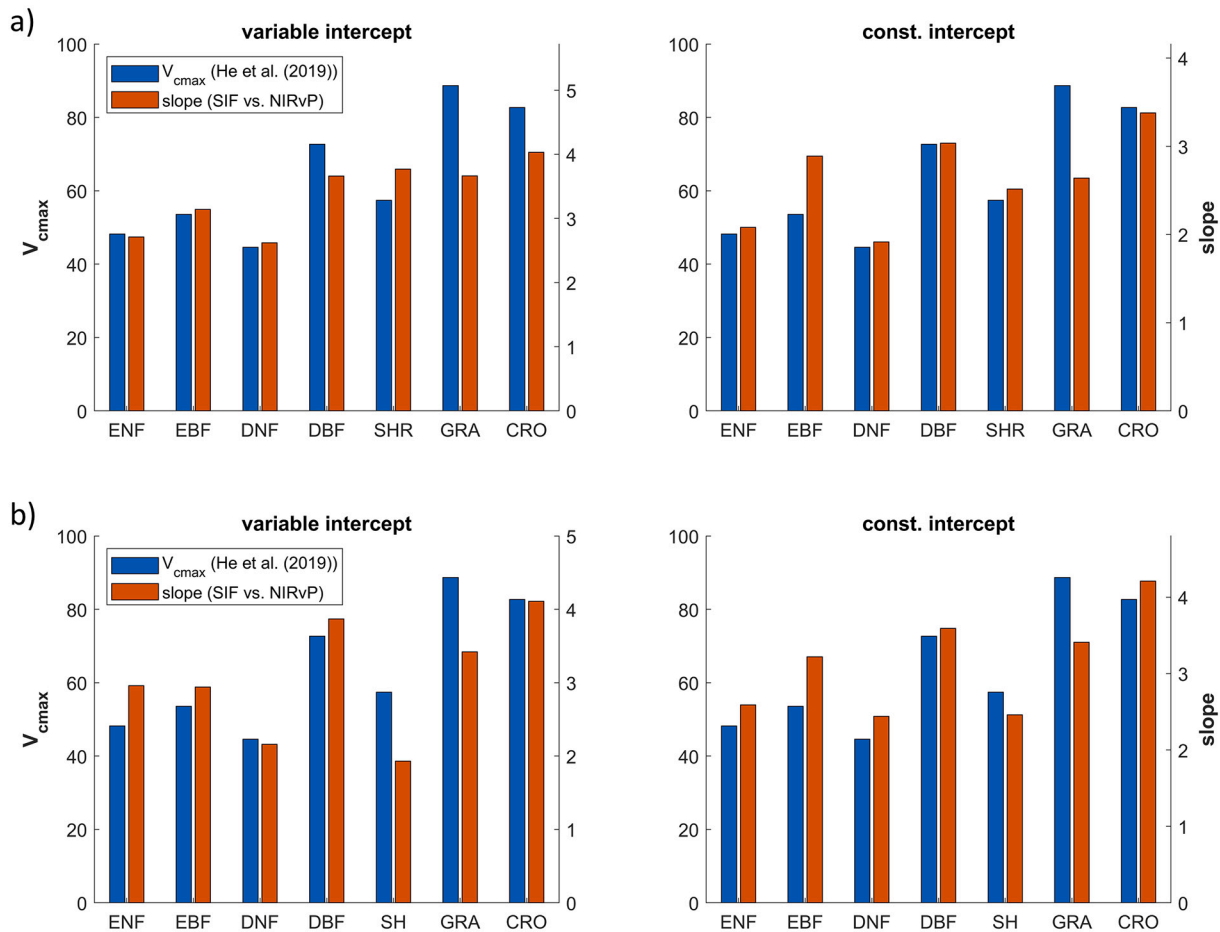


Fig. C1. Comparison of different structural SIF proxies regarding their spatial and temporal correlation to SIF and GPP. Results are based on 8-day, 0.5 degree data in 2018. a) correlation of MODIS-based vegetation indices multiplied by PAR (e.g. NIR<sub>v</sub>P) and APAR to TROPOMI SIF, CSIF, and FLUXCOM GPP. The third row evaluates the effect of vegetation density on the results, the green dashed line is the reference at zero difference in R<sup>2</sup>. (For interpretation of the references to color in this figure legend, the reader is referred to the web version of this article.)

Appendix D. PFT-level patterns of satellite SIF vs. NIR<sub>v</sub>P compared to independent V<sub>cmax</sub>

**Fig. D1.** Comparison of the regression slope of TROPOMI SIF vs. NIR<sub>v</sub>P with independent estimates of V<sub>cmax</sub>. Linear regressions were conducted with either variable intercept or constant intercept per plant function type (PFT). a) Temporal regression based on 8-daily data at 0.5 degree spatial resolution. b) spatial regression based on July average data at 0.05 degree resolution. The constant intercept was calculated as average of median PFT intercepts from the variable intercept results (see Methods). V<sub>cmax</sub> is from He et al. (2019) and denotes the normalized V<sub>cmax</sub> value at 25 °C units of μmol CO<sub>2</sub> m<sup>-2</sup> s<sup>-1</sup>. Although the V<sub>cmax</sub> product we used as reference here is also based on SIF, it used observations from a different sensor (GOME-2) and V<sub>cmax</sub> was derived with an entirely different approach involving a process-based model and data assimilation (He et al., 2019). The value of regression slopes corresponds to SIF is in units of mW m<sup>-2</sup> sr<sup>-1</sup> nm<sup>-1</sup> and NIR<sub>v</sub>P in units of nmol m<sup>-2</sup> s<sup>-1</sup>. PFTs are abbreviated as in Fig. S3.

## References

- Badgley, G., Field, C.B., Berry, J.A., 2017. Canopy near-infrared reflectance and terrestrial photosynthesis. *Sci. Adv.* 3, e1602244.
- Badgley, G., Anderegg, L.D.L., Berry, J.A., Field, C.B., 2019. Terrestrial gross primary production: using NIR<sub>v</sub> to scale from site to globe. *Glob. Chang. Biol.* 25, 3731–3740. <https://doi.org/10.1111/gcb.14729>.
- Baldocchi, D.D., Ryu, Y., Dechant, B., Eichelmann, E., Hemes, K., Ma, S., Rey Sanchez, C., Shortt, R., Szutu, D., Valach, A., Verfaillie, J., Badgley, G., Zeng, Y., Berry, J.A., 2020. Outgoing near infrared radiation from vegetation scales with canopy photosynthesis across a spectrum of function, structure, physiological capacity and weather. *J. Geophys. Res. Biogeosci.* <https://doi.org/10.1029/2019JG005534>.
- Camino, C., Gonzalez-Dugo, V., Hernandez, P., Zarco-Tejada, P.J., 2019. Radiative transfer Vcmax estimation from hyperspectral imagery and SIF retrievals to assess photosynthetic performance in rainfed and irrigated plant phenotyping trials. *Remote Sens. Environ.* 111186. <https://doi.org/10.1016/j.rse.2019.05.005>.
- Chang, C.Y., Guanter, L., Frankenberg, C., Köhler, P., Gu, L., Magney, T.S., Grossmann, K., Sun, Y., 2020. Systematic assessment of retrieval methods for canopy far-red solar-induced chlorophyll fluorescence (SIF) using high-frequency automated field spectroscopy. *J. Geophys. Res. Biogeosci.* <https://doi.org/10.1029/2019JG005533>.
- Cogliati, S., Celesti, M., Cesana, I., Miglietta, F., Genesio, L., Julitta, T., Schuettemeyer, D., Drusch, M., Rascher, U., Jurado, P., Colombo, R., 2019. A spectral fitting algorithm to retrieve the fluorescence spectrum from canopy radiance. *Remote Sens.* 11, 1840. <https://doi.org/10.3390/rs11161840>.
- Croft, H., Chen, J.M., Luo, X., Bartlett, P., Chen, B., Staebler, R.M., 2016. Leaf chlorophyll content as a proxy for leaf photosynthetic capacity. *Glob. Chang. Biol.* <https://doi.org/10.1111/gcb.13599>.
- Croft, H., Chen, J.M., Wang, R., Mo, G., Luo, S., Luo, X., He, L., Gonsamo, A., Arabian, J., Zhang, Y., Simic-Milas, A., Noland, T.L., He, Y., Homolová, L., Malenkovský, Z., Yi, Q., Beringer, J., Amiri, R., Hutley, L., Arellano, P., Stahl, C., Bonal, D., 2020. The global distribution of leaf chlorophyll content. *Remote Sens. Environ.* 236, 111479. <https://doi.org/10.1016/j.rse.2019.111479>.
- Daumard, F., Champagne, S., Fournier, A., Goulas, Y., Ounis, A., Hanocq, J.-F., Moya, I., 2010. A field platform for continuous measurement of canopy fluorescence. *IEEE Trans. Geosci. Remote Sens.* 48, 3358–3368. <https://doi.org/10.1109/TGRS.2010.2046420>.
- Dechant, B., Ryu, Y., Kang, M., 2019. Making full use of hyperspectral data for gross primary productivity estimation with multivariate regression: mechanistic insights from observations and process-based simulations. *Remote Sens. Environ.* 234, 111435. <https://doi.org/10.1016/j.rse.2019.111435>.
- Dechant, B., Ryu, Y., Badgley, G., Zeng, Y., Berry, J.A., Zhang, Y., Goulas, Y., Li, Z., Zhang, Q., Kang, M., Li, J., Moya, I., 2020. Canopy structure explains the relationship between photosynthesis and sun-induced chlorophyll fluorescence in crops. *Remote Sens. Environ.* 241, 111733. <https://doi.org/10.1016/j.rse.2020.111733>.
- Drusch, M., Moreno, J., Del Bello, U., Franco, R., Goulas, Y., Huth, A., Kraft, S., Middleton, E.M., Miglietta, F., Mohammed, G., Nedbal, L., Rascher, U., Schuettemeyer, D., Verhoef, W., 2017. The fluorescence explorer mission concept—ESA's earth explorer 8. *IEEE Trans. Geosci. Remote Sens.* 55, 1273–1284. <https://doi.org/10.1109/TGRS.2016.2621820>.

- Duveiller, G., Filippini, F., Walther, S., Köhler, P., Frankenberg, C., Guanter, L., Cescatti, A., 2019. A spatially downscaled sun-induced fluorescence global product for enhanced monitoring of vegetation productivity. *Earth Syst. Sci. Data Discuss.* 1–24. <https://doi.org/10.5194/essd-2019-121>.
- El-Madany, T.S., 2018. Drivers of spatio-temporal variability of carbon dioxide and energy fluxes in a Mediterranean savanna ecosystem. *Agric. For. Meteorol.* 262, 258–278. <https://doi.org/10.1016/j.agrformet.2018.07.010>.
- Flexas, J., Escalona, J.M., Evain, S., Gullás, J., Moya, I., Osmond, C.B., Medrano, H., 2002. Steady-state chlorophyll fluorescence (Fs) measurements as a tool to follow variations of net CO<sub>2</sub> assimilation and stomatal conductance during water-stress in C<sub>3</sub> plants. *Physiol. Plant.* 114, 231–240.
- Frankenberg, C., Berry, J., 2018. Solar induced chlorophyll fluorescence: origins, relation to photosynthesis and retrieval. In: *Comprehensive Remote Sensing*. Elsevier, pp. 143–162. <https://doi.org/10.1016/B978-0-12-409548-9.10632-3>.
- Gamon, J.A., Penuelas, J., Field, C.B., 1992. A narrow-waveband spectral index that tracks diurnal changes in photosynthetic efficiency. *Remote Sens. Environ.* 41, 35–44.
- Gitelson, A.A., Gamon, J.A., 2015. The need for a common basis for defining light-use efficiency: implications for productivity estimation. *Remote Sens. Environ.* 156, 196–201. <https://doi.org/10.1016/j.rse.2014.09.017>.
- Goulas, Y., Fournier, A., Daumard, F., Champagne, S., Ounis, A., Marloie, O., Moya, I., 2017. Gross primary production of a wheat canopy relates stronger to far red than to red solar-induced chlorophyll fluorescence. *Remote Sens.* 9, 97. <https://doi.org/10.3390/rs9010097>.
- Gu, L., Han, J., Wood, J.D., Chang, C.Y., Sun, Y., 2019. Sun-induced Chl fluorescence and its importance for biophysical modeling of photosynthesis based on light reactions. *New Phytol.* 223 (3), 1179–1191. <https://doi.org/10.1111/nph.15796>.
- Guan, K., Pan, M., Li, H., Wolf, A., Wu, J., Medvigy, D., Caylor, K.K., Sheffield, J., Wood, E.F., Malhi, Y., Liang, M., Kimball, J.S., Saleska, S.R., Berry, J., Joiner, J., Lyapustin, A.I., 2015. Photosynthetic seasonality of global tropical forests constrained by hydroclimate. *Nat. Geosci.* 8, 284–289. <https://doi.org/10.1038/ngeo2382>.
- Guan, K., Berry, J.A., Zhang, Y., Joiner, J., Guanter, L., Badgley, G., Lobell, D.B., 2016. Improving the monitoring of crop productivity using spaceborne solar-induced fluorescence. *Glob. Chang. Biol.* 22, 716–726. <https://doi.org/10.1111/gcb.13136>.
- Guanter, L., Rossini, M., Colombo, R., Meroni, M., Frankenberg, C., Lee, J.-E., Joiner, J., 2013. Using field spectroscopy to assess the potential of statistical approaches for the retrieval of sun-induced chlorophyll fluorescence from ground and space. *Remote Sens. Environ.* 133, 52–61. <https://doi.org/10.1016/j.rse.2013.01.017>.
- Guanter, L., Zhang, Y., Jung, M., Joiner, J., Voigt, M., Berry, J.A., Frankenberg, C., Huete, A.R., Zarco-Tejada, P., Lee, J.-E., Moran, M.S., Ponce-Campos, G., Beer, C., Camps-Valls, G., Buchmann, N., Gianelle, D., Klumpp, K., Cescatti, A., Baker, J.M., Griffis, T.J., 2014. Global and time-resolved monitoring of crop photosynthesis with chlorophyll fluorescence. *Proc. Natl. Acad. Sci.* 111, E1327–E1333. <https://doi.org/10.1073/pnas.1320008111>.
- Hao, D., Asrar, G.R., Zeng, Y., Zhu, Q., Wen, J., Xiao, Q., Chen, M., 2019. Estimating hourly land surface downward shortwave and photosynthetically active radiation from DSCOVR/EPIC observations. *Remote Sens. Environ.* 232, 111320. <https://doi.org/10.1016/j.rse.2019.111320>.
- He, L., Chen, J.M., Liu, J., Zheng, T., Wang, R., Joiner, J., Chou, S., Chen, B., Liu, Y., Liu, R., Rogers, C., 2019. Diverse photosynthetic capacity of global ecosystems mapped by satellite chlorophyll fluorescence measurements. *Remote Sens. Environ.* 232, 111344. <https://doi.org/10.1016/j.rse.2019.111344>.
- He, L., Magney, T., Dutta, D., Yin, Y., Köhler, P., Grossmann, K., Stutz, J., Dold, C., Hatfield, J., Guan, K., Peng, B., Frankenberg, C., 2020. From the ground to space: using solar-induced chlorophyll fluorescence to estimate crop productivity. *Geophys. Res. Lett.* 47. <https://doi.org/10.1029/2020GL087474>.
- Huete, A., Didan, K., Miura, T., Rodriguez, E.P., Gao, X., Ferreira, L.G., 2002. Overview of the radiometric and biophysical performance of the MODIS vegetation indices. *Remote Sens. Environ.* 83, 195–213. [https://doi.org/10.1016/S0034-4257\(02\)00096-2](https://doi.org/10.1016/S0034-4257(02)00096-2).
- Jiang, Z., Huete, A., Didan, K., Miura, T., 2008. Development of a two-band enhanced vegetation index without a blue band. *Remote Sens. Environ.* 112, 3833–3845. <https://doi.org/10.1016/j.rse.2008.06.006>.
- Jiang, C., Guan, K., Wu, G., Peng, B., Wang, S., 2020. A daily, 250 m, and real-time gross primary productivity product (2000-present) covering the contiguous United States (preprint). *Biosph. Biogeosci.* <https://doi.org/10.5194/essd-2020-36>.
- Joiner, J., Guanter, L., Lindstrot, R., Voigt, M., Vasilkov, A.P., Middleton, E.M., Huemmrich, K.F., Yoshida, Y., Frankenberg, C., 2013. Global monitoring of terrestrial chlorophyll fluorescence from moderate-spectral-resolution near-infrared satellite measurements: methodology, simulations, and application to GOME-2. *Atmos. Meas. Tech.* 6, 2803–2823. <https://doi.org/10.5194/amt-6-2803-2013>.
- Joiner, J., Yoshida, Y., Köhler, P., Campbell, P., Frankenberg, C., van der Tol, C., Yang, P., Parazoo, N., Guanter, L., Sun, Y., 2020. Systematic orbital geometry-dependent variations in satellite solar-induced fluorescence (SIF) retrievals. *Remote Sens.* 12, 2346. <https://doi.org/10.3390/rs12152346>.
- Jonard, F., De Cannière, S., Brüggemann, N., Gentine, P., Short Gianotti, D.J., Lobet, G., Miralles, D.G., Montzka, C., Pagán, B.R., Rascher, U., Vereecken, H., 2020. Value of sun-induced chlorophyll fluorescence for quantifying hydrological states and fluxes: current status and challenges. *Agric. For. Meteorol.* 291, 108088. <https://doi.org/10.1016/j.agrformet.2020.108088>.
- Jung, M., Koirala, S., Weber, U., Ichii, K., Gans, F., Camps-Valls, G., Reichstein, M., 2019. The FLUXCOM ensemble of global land-atmosphere energy fluxes. *Scientific data* 6 (1), 1–14.
- Jung, M., Schwalm, C., Migliavacca, M., Walther, S., Camps-Valls, G., Koirala, S., Anthoni, P., Besnard, S., Bodesheim, P., Carvalhais, N., Chevallier, F., Gans, F., Goll, D.S., Haverd, V., Köhler, P., Ichii, K., Jain, A.K., Liu, J., Lombardozi, D., Nabel, J.E.M.S., Nelson, J.A., O’ Sullivan, M., Pallandt, M., Papale, D., Peters, W., Pongratz, J., Rödenbeck, C., Sitch, S., Tramontana, G., Walker, A., Weber, U., Reichstein, M., 2020. Scaling carbon fluxes from eddy covariance sites to globe: synthesis and evaluation of the FLUXCOM approach. *Biogeosciences* 17, 1343–1365. <https://doi.org/10.5194/bg-17-1343-2020>.
- Kim, J., Ryu, Y., Jiang, C., Hwang, Y., 2019. Continuous observation of vegetation canopy dynamics using an integrated low-cost, near-surface remote sensing system. *Agric. For. Meteorol.* 264, 164–177. <https://doi.org/10.1016/j.agrformet.2018.09.014>.
- Kim, J., Ryu, Y., Dechant, B., Lee, H., Kim, H.S., Kornfeld, A., Berry, J.A., 2021. Solar-induced chlorophyll fluorescence is non-linearly related to canopy photosynthesis in a temperate evergreen needleleaf forest during the fall transition. *Remote Sens. Environ.* 258, 112362. <https://doi.org/10.1016/j.rse.2021.112362>.
- Köhler, P., Guanter, L., Joiner, J., 2015. A linear method for the retrieval of sun-induced chlorophyll fluorescence from GOME-2 and SCIAMACHY data. *Atmos. Meas. Tech.* 8, 2589–2608. <https://doi.org/10.5194/amt-8-2589-2015>.
- Köhler, P., Frankenberg, C., Magney, T.S., Guanter, L., Joiner, J., Landgraf, J., 2018. Global retrievals of solar-induced chlorophyll fluorescence with TROPOMI: first results and Intersensor comparison to OCO-2. *Geophys. Res. Lett.* <https://doi.org/10.1029/2018GL079031>.
- Lee, J.-E., Berry, J.A., van der Tol, C., Yang, X., Guanter, L., Damm, A., Baker, I., Frankenberg, C., 2015. Simulations of chlorophyll fluorescence incorporated into the community land model version 4. *Glob. Chang. Biol.* 21, 3469–3477. <https://doi.org/10.1111/gcb.12948>.
- Li, X., Xiao, J., 2020. Global climatic controls on interannual variability of ecosystem productivity: similarities and differences inferred from solar-induced chlorophyll fluorescence and enhanced vegetation index. *Agric. For. Meteorol.* 288–289, 108018. <https://doi.org/10.1016/j.agrformet.2020.108018>.
- Li, Z., Zhang, Q., Li, J., Yang, X., Wu, Y., Zhang, Z., Wang, S., Wang, H., Zhang, Y., 2020. Solar-induced chlorophyll fluorescence and its link to canopy photosynthesis in maize from continuous ground measurements. *Remote Sens. Environ.* 236, 111420. <https://doi.org/10.1016/j.rse.2019.111420>.
- Liu, L., Liu, X., Chen, J., Du, S., Ma, Y., Qian, X., Chen, S., Peng, D., 2020. Estimating Maize GPP using near-infrared radiance of vegetation. *Sci. Remote Sens.* 100009. <https://doi.org/10.1016/j.srs.2020.100009>.
- Magney, T.S., Bowling, D.R., Logan, B.A., Grossmann, K., Stutz, J., Blanken, P.D., Burns, S.P., Cheng, R., Garcia, M.A., Köhler, P., Lopez, S., Parazoo, N.C., Raczka, B., Schimel, D., Frankenberg, C., 2019. Mechanistic evidence for tracking the seasonality of photosynthesis with solar-induced fluorescence. *Proc. Natl. Acad. Sci.* 201900278. <https://doi.org/10.1073/pnas.1900278116>.
- Marrs, J.K., Jones, T.S., Allen, D.W., Hutyrá, L.R., 2021. Instrumentation sensitivities for tower-based solar-induced fluorescence measurements. *Remote Sens. Environ.* 259, 112413. <https://doi.org/10.1016/j.rse.2021.112413>.
- Martini, D., Pacheco-Labrador, Javier, Perez-Priego, Oscar, van der Tol, C., El-Madany, Tarek S., Julitta, Tommaso, Rossini, Micol, Reichstein, Markus, Christiansen, Rune, Rascher, Uwe, Moreno, Gerardo, Martín, M. Pilar, Yang, Peiqi, Carrara, Arnaud, Guan, Jinhong, González-Casón, Rosario, Migliavacca, Mirco, 2019. Nitrogen and phosphorus effect on sun-induced fluorescence and gross primary productivity in Mediterranean grassland. *Remote Sens.* 11, 2562. <https://doi.org/10.3390/rs11212562>.
- Meroni, M., Colombo, R., 2006. Leaf level detection of solar induced chlorophyll fluorescence by means of a subnanometer resolution spectroradiometer. *Remote Sens. Environ.* 103, 438–448. <https://doi.org/10.1016/j.rse.2006.03.016>.
- Miao, G., Guan, K., Yang, X., Bernacchi, C.J., Berry, J.A., DeLucia, E.H., Wu, J., Moore, C. E., Meacham, K., Cai, Y., Peng, B., Kimm, H., Masters, M.D., 2018. Sun-induced chlorophyll fluorescence, photosynthesis, and light use efficiency of a soybean field from seasonally continuous measurements. *J. Geophys. Res. Biogeosci.* 123, 610–623. <https://doi.org/10.1002/2017JG004180>.
- Migliavacca, M., Perez-Priego, O., Rossini, M., El-Madany, T.S., Moreno, G., van der Tol, C., Rascher, U., Berninger, A., Bessenbacher, V., Burkart, A., Carrara, A., Fava, F., Guan, J.-H., Hammer, T.W., Henkel, K., Juarez-Alcalde, E., Julitta, T., Kolle, O., Martín, M.P., Musavi, T., Pacheco-Labrador, J., Pérez-Burguño, A., Wutzler, T., Zaehle, S., Reichstein, M., 2017. Plant functional traits and canopy structure control the relationship between photosynthetic CO<sub>2</sub> uptake and far-red sun-induced fluorescence in a Mediterranean grassland under different nutrient availability. *New Phytol.* <https://doi.org/10.1111/nph.14437>.
- Mohammed, G.H., Colombo, R., Middleton, E.M., Rascher, U., van der Tol, C., Nedbal, L., Goulas, Y., Pérez-Priego, O., Damm, A., Meroni, M., Joiner, J., Cogliati, S., Verhoef, W., Malenovsky, Z., Gastellu-Etchegorry, J.-P., Miller, J.R., Guanter, L., Moreno, J., Moya, I., Berry, J.A., Frankenberg, C., Zarco-Tejada, P.J., 2019. Remote sensing of solar-induced chlorophyll fluorescence (SIF) in vegetation: 50 years of progress. *Remote Sens. Environ.* 231, 111177. <https://doi.org/10.1016/j.rse.2019.04.030>.
- Peng, B., Guan, K., Zhou, W., Jiang, C., Frankenberg, C., Sun, Y., He, L., Köhler, P., 2020. Assessing the benefit of satellite-based solar-induced chlorophyll fluorescence in crop yield prediction. *Int. J. Appl. Earth Obs. Geoinf.* 90, 102126. <https://doi.org/10.1016/j.jag.2020.102126>.
- Porcar-Castell, A., 2011. A high-resolution portrait of the annual dynamics of photochemical and non-photochemical quenching in needles of *Pinus sylvestris*. *Physiol. Plant.* 143, 139–153. <https://doi.org/10.1111/j.1399-3054.2011.01488.x>.
- Porcar-Castell, A., Tyystjärvi, E., Atherton, J., van der Tol, C., Flexas, J., Pfundel, E.E., Moreno, J., Frankenberg, C., Berry, J.A., 2014. Linking chlorophyll a fluorescence to photosynthesis for remote sensing applications: mechanisms and challenges. *J. Exp. Bot.* 65, 4065–4095. <https://doi.org/10.1093/jxb/eru191>.

- Qiu, B., Xue, Y., Fisher, J.B., Guo, W., Berry, J.A., Zhang, Y., 2018. Satellite chlorophyll fluorescence and soil moisture observations lead to advances in the predictive understanding of global terrestrial coupled carbon-water cycles. *Glob. Biogeochem. Cycles* 32, 360–375. <https://doi.org/10.1002/2017GB005744>.
- Qiu, B., Chen, J.M., Ju, W., Zhang, Q., Zhang, Y., 2019. Simulating emission and scattering of solar-induced chlorophyll fluorescence at far-red band in global vegetation with different canopy structures. *Remote Sens. Environ.* 233, 111373. <https://doi.org/10.1016/j.rse.2019.111373>.
- Qiu, B., Ge, J., Guo, W., Pitman, A.J., Mu, M., 2020. Responses of Australian dryland vegetation to the 2019 heatwave at a sub-daily scale. *Geophys. Res. Lett.* <https://doi.org/10.1029/2019GL086569>.
- Rascher, U., Alonso, L., Burkart, A., Cilia, C., Cogliati, S., Colombo, R., Damm, A., Drusch, M., Guanter, L., Hanus, J., Hyvärinen, T., Julitta, T., Jussila, J., Kataja, K., Kokkalis, P., Kraft, S., Kraska, T., Matveeva, M., Moreno, J., Müller, O., Panigada, C., Píkl, M., Pinto, F., Prey, L., Pude, R., Rossini, M., Schickling, A., Schurr, U., Schüttemeyer, D., Verrelst, J., Zemek, F., 2015. Sun-induced fluorescence - a new probe of photosynthesis: first maps from the imaging spectrometer *HyPlant*. *Glob. Chang. Biol.* 21, 4673–4684. <https://doi.org/10.1111/gcb.13017>.
- Rouse, J.W., Haas, R.H., Schell, J.A., Deering, D.W., 1974. Monitoring vegetation systems in the Great Plains with ERTS. In: *Third ERTS Symp. NASA SP-351 1*, pp. 309–317.
- Ryu, Y., Jiang, C., Kobayashi, H., Detto, M., 2018. MODIS-derived global land products of shortwave radiation and diffuse and total photosynthetically active radiation at 5 km resolution from 2000. *Remote Sens. Environ.* 204, 812–825. <https://doi.org/10.1016/j.rse.2017.09.021>.
- Ryu, Y., Berry, J.A., Baldocchi, D.D., 2019. What is global photosynthesis? History, uncertainties and opportunities. *Remote Sens. Environ.* 223, 95–114. <https://doi.org/10.1016/j.rse.2019.01.016>.
- Siddans, R., 2017. *S5p-NPP Cloud Processor ATBD*. Rutherford Appleton Lab, Didcot UK.
- Siegmann, B., 2019. The High-Performance Airborne Imaging Spectrometer *HyPlant* – From Raw Images to Top-of-Canopy Reflectance and Fluorescence products: an Example Dataset from the Agricultural Researchstation Campus Klein-Altendorf. <https://doi.org/10.5447/IPK/2019/21>.
- Siegmann, B., Alonso, L., Celesti, M., Cogliati, S., Colombo, R., Damm, A., Douglas, S., Guanter, L., Hanus, J., Kataja, K., Kraska, T., Matveeva, M., Moreno, J., Müller, O., Píkl, M., Pinto, F., Quirós Vargas, J., Rademske, P., Rodríguez-Moreno, F., Sabater, N., Schickling, A., Schüttemeyer, D., Zemek, F., Rascher, U., 2019. The high-performance airborne imaging spectrometer *HyPlant*—from raw images to top-of-canopy reflectance and fluorescence products: introduction of an automatized processing chain. *Remote Sens.* 11, 2760. <https://doi.org/10.3390/rs11232760>.
- Sims, D.A., Rahman, A.F., Vermote, E.F., Jiang, Z., 2011. Seasonal and inter-annual variation in view angle effects on MODIS vegetation indices at three forest sites. *Remote Sens. Environ.* 115, 3112–3120. <https://doi.org/10.1016/j.rse.2011.06.018>.
- Somkuti, P., Bösch, H., Feng, L., Palmer, P.I., Parker, R.J., Quaife, T., 2020. A new space-borne perspective of crop productivity variations over the US Corn Belt. *Agric. For. Meteorol.* 281, 107826. <https://doi.org/10.1016/j.agrformet.2019.107826>.
- Sun, Y., Frankenberg, C., Wood, J.D., Schimel, D.S., Jung, M., Guanter, L., Drewry, D.T., Verma, M., Porcar-Castell, A., Griffis, T.J., Gu, L., Magney, T.S., Köhler, P., Evans, B., Yuen, K., 2017. OCO-2 advances photosynthesis observation from space via solar-induced chlorophyll fluorescence. *Science* 358. <https://doi.org/10.1126/science.aam5747>.
- Tagliabue, G., Panigada, C., Celesti, M., Cogliati, S., Colombo, R., Migliavacca, M., Rascher, U., Rocchini, D., Schüttemeyer, D., Rossini, M., 2020. Sun-induced fluorescence heterogeneity as a measure of functional diversity. *Remote Sens. Environ.* 247, 111934. <https://doi.org/10.1016/j.rse.2020.111934>.
- Tucker, C.J., 1979. Red and photographic infrared linear combinations for monitoring vegetation. *Remote Sens. Environ.* 8, 127–150.
- Tucker, C.J., Myneni, R.B., Shabanov, V., Knyazikhin, Y., Zhou, L., Kaufmann, R.K., 2000. Effect of orbital drift and sensor changes on the time series of AVHRR vegetation index data. *IEEE Trans. Geosci. Remote Sens.* 38, 2584–2597. <https://doi.org/10.1109/36.885205>.
- Turner, A.J., Köhler, P., Magney, T.S., Frankenberg, C., Fung, I., Cohen, R.C., 2019. A double peak in the seasonality of California's photosynthesis as observed from space (preprint). *Biogeochemistry*. <https://doi.org/10.5194/bg-2019-387>.
- van der Tol, C., Verhoef, W., Timmermans, J., Verhoef, A., Su, Z., 2009. An integrated model of soil-canopy spectral radiances, photosynthesis, fluorescence, temperature and energy balance. *Biogeosciences* 6, 3109–3129. <https://doi.org/10.5194/bg-6-3109-2009>.
- van der Tol, C., Berry, J.A., Campbell, P.K.E., Rascher, U., 2014. Models of fluorescence and photosynthesis for interpreting measurements of solar-induced chlorophyll fluorescence. *J. Geophys. Res. Biogeosci.* 119, 2312–2327. <https://doi.org/10.1002/2014JG002713>.
- Veefkind, J.P., Aben, I., McMullan, K., Förster, H., de Vries, J., Otter, G., Claas, J., Eskes, H.J., de Haan, J.F., Kleipool, Q., van Weele, M., Hasekamp, O., Hoogeveen, R., Landgraf, J., Snel, R., Tol, P., Ingmann, P., Voors, R., Krüzinga, B., Vink, R., Visser, H., Levelt, P.F., 2012. TROPOMI on the ESA Sentinel-5 precursor: A GEMS mission for global observations of the atmospheric composition for climate, air quality and ozone layer applications. *Remote Sens. Environ.* 120, 70–83. <https://doi.org/10.1016/j.rse.2011.09.027>.
- Verrelst, J., Schaepman, M.E., Koetz, B., Kneubühler, M., 2008. Angular sensitivity analysis of vegetation indices derived from CHRIS/PROBA data. *Remote Sens. Environ.* 112, 2341–2353. <https://doi.org/10.1016/j.rse.2007.11.001>.
- Vilfan, N., van der Tol, C., Müller, O., Rascher, U., Verhoef, W., 2016. FluSpec-B: A model for leaf fluorescence, reflectance and transmittance spectra. *Remote Sens. Environ.* 186, 596–615. <https://doi.org/10.1016/j.rse.2016.09.017>.
- Walther, S., Voigt, M., Thum, T., Gonsamo, A., Zhang, Y., Koehler, P., Jung, M., Varlagin, A., Guanter, L., 2015. Satellite chlorophyll fluorescence measurements reveal large-scale decoupling of photosynthesis and greenness dynamics in boreal evergreen forests. *Glob. Chang. Biol.* <https://doi.org/10.1111/gcb.13200> n/a-n/a.
- Wang, C., Guan, K., Peng, B., Chen, M., Jiang, C., Zeng, Y., Wu, G., Wang, S., Wu, J., Yang, X., Frankenberg, C., Köhler, P., Berry, J., Bernacchi, C., Zhu, K., Alden, C., Miao, G., 2020. Satellite footprint data from OCO-2 and TROPOMI reveal significant spatio-temporal and inter-vegetation type variabilities of solar-induced fluorescence yield in the U.S. Midwest. *Remote Sens. Environ.* 241, 111728. <https://doi.org/10.1016/j.rse.2020.111728>.
- Wen, J., Köhler, P., Duveiller, G., Parazoo, N.C., Magney, T.S., Hooker, G., Yu, L., Chang, C.Y., Sun, Y., 2020. A framework for harmonizing multiple satellite instruments to generate a long-term global high spatial-resolution solar-induced chlorophyll fluorescence (SIF). *Remote Sens. Environ.* 239, 111644. <https://doi.org/10.1016/j.rse.2020.111644>.
- Wieneke, S., Burkart, A., Cendrero-Mateo, M.P., Julitta, T., Rossini, M., Schickling, A., Schmidt, M., Rascher, U., 2018. Linking photosynthesis and sun-induced fluorescence at sub-daily to seasonal scales. *Remote Sens. Environ.* 219, 247–258. <https://doi.org/10.1016/j.rse.2018.10.019>.
- Wohlfahrt, G., Gerdel, K., Migliavacca, M., Rotenberg, E., Tatarinov, F., Müller, J., Hammerle, A., Julitta, T., Spielmann, F.M., Yakir, D., 2018. Sun-induced fluorescence and gross primary productivity during a heat wave. *Sci. Rep.* 8 <https://doi.org/10.1038/s41598-018-32602-z>.
- Wu, G., Guan, K., Jiang, C., Peng, B., Kimm, H., Chen, M., Yang, X., Wang, S., Sukyer, A. E., Bernacchi, C., Moore, C.E., Zeng, Y., Berry, J., Cendrero-Mateo, M.P., 2019. Radiance-based NIR<sub>v</sub> as a proxy for GPP of corn and soybean. *Environ. Res. Lett.* <https://doi.org/10.1088/1748-9326/ab65cc>.
- Xu, S., Atherton, J., Riikonen, A., Zhang, C., Oivukkamäki, J., MacArthur, A., Honkavaara, E., Hakala, T., Koivumäki, N., Liu, Z., Porcar-Castell, A., 2021. Structural and photosynthetic dynamics mediate the response of SIF to water stress in a potato crop. *Remote Sens. Environ.* 263, 112555. <https://doi.org/10.1016/j.rse.2021.112555>.
- Yang, P., van der Tol, C., 2018. Linking canopy scattering of far-red sun-induced chlorophyll fluorescence with reflectance. *Remote Sens. Environ.* 209, 456–467. <https://doi.org/10.1016/j.rse.2018.02.029>.
- Yang, X., Tang, J., Mustard, J.F., Lee, J.-E., Rossini, M., Joiner, J., Munger, J.W., Kornfeld, A., Richardson, A.D., 2015. Solar-induced chlorophyll fluorescence that correlates with canopy photosynthesis on diurnal and seasonal scales in a temperate deciduous forest: fluorescence and photosynthesis. *Geophys. Res. Lett.* 42, 2977–2987. <https://doi.org/10.1002/2015GL063201>.
- Yang, K., Ryu, Y., Dechant, B., Berry, J.A., Hwang, Y., Jiang, C., Kang, M., Kim, J., Kimm, H., Kornfeld, A., Yang, X., 2018. Sun-induced chlorophyll fluorescence is more strongly related to absorbed light than to photosynthesis at half-hourly resolution in a rice paddy. *Remote Sens. Environ.* 216, 658–673. <https://doi.org/10.1016/j.rse.2018.07.008>.
- Yang, X., Shi, H., Stovall, A., Guan, K., Miao, G., Zhang, Yongguang, Zhang, Yao, Xiao, X., Ryu, Y., Lee, J.-E., 2018. FluSpec 2—An Automated Field Spectroscopy System to Monitor Canopy Solar-Induced Fluorescence, 18.
- Yang, P., van der Tol, C., Campbell, P.K.E., Middleton, E.M., 2020. Fluorescence correction vegetation index (FCVI): A physically based reflectance index to separate physiological and non-physiological information in far-red sun-induced chlorophyll fluorescence. *Remote Sens. Environ.* 240, 111676. <https://doi.org/10.1016/j.rse.2020.111676>.
- Zeng, Y., Badgley, G., Dechant, B., Ryu, Y., Chen, M., Berry, J.A., 2019. A practical approach for estimating the escape ratio of near-infrared solar-induced chlorophyll fluorescence. *Remote Sens. Environ.* 232, 111209. <https://doi.org/10.1016/j.rse.2019.05.028>.
- Zhang, Y., Guanter, L., Berry, J.A., Joiner, J., van der Tol, C., Huete, A., Gitelson, A., Voigt, M., Köhler, P., 2014. Estimation of vegetation photosynthetic capacity from space-based measurements of chlorophyll fluorescence for terrestrial biosphere models. *Glob. Chang. Biol.* 20, 3727–3742. <https://doi.org/10.1111/gcb.12664>.
- Zhang, Y., Joiner, J., Alemohammad, S.H., Zhou, S., Gentine, P., 2018. A global spatially continuous solar induced fluorescence (CSIF) dataset using neural networks. *Biogeosci. Discuss.* 1–34. <https://doi.org/10.5194/bg-2018-255>.
- Zhang, Z., Zhang, Y., Porcar-Castell, A., Joiner, J., Guanter, L., Yang, X., Migliavacca, M., Ju, W., Sun, Z., Chen, S., Martini, D., Zhang, Q., Li, Z., Cleverly, J., Wang, H., Goulas, Y., 2020a. Reduction of structural impacts and distinction of photosynthetic pathways in a global estimation of GPP from space-borne solar-induced chlorophyll fluorescence. *Remote Sens. Environ.* 240, 111722. <https://doi.org/10.1016/j.rse.2020.111722>.
- Zhang, Z., Zhang, Yongguang, Zhang, Yao, Gobron, N., Frankenberg, C., Wang, S., Li, Z., 2020b. The potential of satellite FPAR product for GPP estimation: an indirect evaluation using solar-induced chlorophyll fluorescence. *Remote Sens. Environ.* 240, 111686. <https://doi.org/10.1016/j.rse.2020.111686>.